Atmos. Chem. Phys. Discuss., 13, 30765–30839, 2013
www.atmos-chem-phys-discuss.net/13/30765/2013/
doi:10.5194/acpd-13-30765-2013

Atmospheric Chemistry and Physics Discussions

H_2O and HCl trace gas kinetics on crystalline and amorphous HCl hydrates in the range 170 to 205 K: the HCl/H_2O phase diagram revisited

R. Iannarelli and M. J. Rossi

Laboratory of Atmospheric Chemistry (LAC), Paul Scherrer Institute (PSI), PSI Villigen, 5232, Switzerland

Received: 7 November 2013 – Accepted: 14 November 2013 – Published: 27 November 2013

Correspondence to: M. J. Rossi (michel.rossi@psi.ch)

Published by Copernicus Publications on behalf of the European Geosciences Union.

Abstract

In this laboratory study, H_2O ice films of 1 to 2 µm thickness have been used as surrogates for ice particles at atmospherically relevant conditions in a stirred flow reactor (SFR) to measure the kinetics of evaporation and condensation of HCl and H_2O on crystalline and amorphous HCl hydrates. A multidiagnostic approach has been employed using FTIR absorption spectroscopy in transmission to monitor the condensed phase and residual gas mass spectrometry (MS) for the gas phase. An average mass balance ratio between HCl adsorbed onto ice and the quantity of HCl measured using FTIR absorption, $(N_{in} - N_{esc} - N_{ads})/N^{FTIR} = 1.182 \pm 0.123$ has been obtained. The rate of evaporation R_{ev}(HCl) for crystalline HCl hexahydrate ($HCl \cdot 6H_2O$) films and amorphous HCl/H_2O mixtures has been found to be lower by a factor of 10 to 250 compared to $R_{ev}(H_2O)$ in the overlapping temperature range 175 to 190 K. Variations of the accommodation coefficient α(HCl) on pure $HCl \cdot 6H_2O$ up to a factor of 10 have been observed. The kinetic parameters are thermochemically consistent with the corresponding equilibrium vapour pressure. In addition, we propose an extension of the HCl/H_2O phase diagram of crystalline $HCl \cdot 6H_2O$ based on the analysis of deconvoluted FTIR spectra of samples outside its known existence area. A brief evaluation of the atmospheric importance of both condensed phases, amorphous HCl/H_2O and crystalline $HCl \cdot 6H_2O$, is performed in favour of the amorphous phase.

1 Introduction

After the discovery of the ozone hole over Antarctica, the importance of heterogeneous chemistry on ice surfaces had started to be recognized (Solomon et al., 1986) as well as the role of Polar Stratospheric Clouds (PSCs) as substrates on whose surfaces heterogeneous reactions may take place.

PSC's are formed in the stratosphere during polar night when the temperatures drop to as low as 183 K to allow for cloud formation even in the dry stratosphere (Peter,

ACPD
13, 30765–30839, 2013

1997). PSC's are classified according to their composition, consisting either of crystalline NAT (type Ia), ternary $H_2SO_4/HNO_3/H_2O$ supercooled solution (type Ib) or pure H_2O ice (type II) (Zondlo et al., 2000).

Heterogeneous reactions occurring on PSC's convert the major unreactive chlorine reservoir compounds, $ClONO_2$ and HCl, into molecular chlorine, which is rapidly photolyzed into atomic chlorine. Reaction (R1) is the most important chlorine-activating reaction in the polar stratosphere because it converts two moles of unreactive chlorine compounds into two moles of atomic chlorine after photolysis in an efficient heterogeneous reaction (Seinfeld and Pandis, 2006):

$$ClONO_2(g) + HCl(s) \rightarrow Cl_2(g) + HNO_3(s) \quad \text{(R1)}$$

Reaction (R1) belongs to one of the fastest stratospheric reactions (Friedl et al., 1986; Molina et al., 1985, 1987), orders of magnitude faster than the corresponding homogeneous gas phase process (Molina et al., 1985). The Cl_2 released in the gas phase from Reaction (R1) rapidly photolyzes into free Cl atoms which then establish a rapid cycle of O_3 destruction. Furthermore, Reaction (R1) also leads to the overall removal of nitrogen oxides from the gas phase, trapping HNO_3 in the ice and thus facilitating O_3 destruction through a catalytic cycle as reported in Reactions (R2)–(R4):

$$X + O_3 \rightarrow XO + O_2 \quad \text{(R2)}$$

$$XO + O \rightarrow X + O_2 \quad \text{(R3)}$$

$$\text{net}: O_3 + O \rightarrow O_2 + O_2 \quad \text{(R4)}$$

where X is H, OH, NO, Cl or Br leading to HO_x, NO_x, ClO_x and BrO_x catalytic cycles, respectively.

The understanding of the interaction of HCl with ice is crucial in order to determine the availability of HCl at the gas-ice condensed phase interface for Reaction (R1) to effectively happen. To this purpose, the HCl/ice system has been extensively studied over the years by means of different techniques. Laminar flow tubes and Knudsen

ACPD
13, 30765–30839, 2013

reactors are among the most widely used devices when coupled with diagnostic techniques such as ellipsometry (McNeill et al., 2006), Fourier Transform Infrared (FTIR) spectroscopy in transmission (Ritzhaupt and Devlin, 1991; Koehler et al., 1993; Delzeit et al., 1993) and Reflection-Absorption Infrared Spectroscopy (RAIRS) (Banham et al., 1996; Graham and Roberts, 1997). Two crystalline hydrates have been found at temperatures that may be relevant for the upper troposphere and lower stratosphere, the hexahydrate ($HCl \cdot 6H_2O$) and the trihydrate ($HCl \cdot 3H_2O$). Moreover, amorphous mixtures of variable H_2O : HCl ratios, may well be relevant at stratospheric conditions.

The phase diagram of the HCl/H_2O system constructed by Molina and coworkers (Molina, 1994; Wooldridge et al., 1995) indicates that the HCl trihydrate requires HCl concentrations much higher than found in the stratosphere ([HCl] = 1–3 ppb, Carslaw et al., 1997) and therefore has no atmospheric relevance. On the other hand, HCl hexahydrate may nucleate at HCl concentrations of atmospheric relevance but at temperatures lower than normally found during polar nights such that its atmospheric relevance has been questioned as well (Koehler et al., 1993; McNeill et al., 2007; Chiesa and Rossi, 2013). It thus appears that only amorphous HCl/H_2O mixtures have atmospheric relevance which are in addition more reactive than the crystalline phase $HCl \cdot 6H_2O$ as far as Reaction (R1) is concerned (McNeill et al., 2006, 2007).

In this study we focused our attention on the HCl hexahydrate phase as well as on amorphous mixtures of concentrations comparable to HCl hexahydrate in order to compare its behaviour under typical stratospheric conditions of [H_2O] = 2–6 ppm and [HCl] = 1–3 ppb (Carslaw et al., 1997). Our results are in agreement with previous studies in showing that the irreversible conversion of HCl hexahydrate into an amorphous 6 : 1 H_2O : HCl mixture occurred at temperatures higher than 190 K (Graham and Roberts, 1997; Sadtchenko et al., 2000; Chiesa and Rossi, 2013) and that the amorphous HCl/H_2O phase had a higher reactivity compared to the crystalline $HCl \cdot 6H_2O$ under similar HCl and H_2O vapour pressures (McNeill et al., 2006; Chiesa and Rossi, 2013).

ACPD
13, 30765–30839, 2013

The main focus of this study is, however, the heterogeneous kinetics of H_2O and HCl interacting with crystalline HCl hexahydrate and amorphous HCl/H_2O phases which have, to our knowledge, not been studied in detail before. The majority of studies focus on the HCl interaction with ice in terms of the total uptake on pure ice films (Abbatt et al., 1992; Hanson and Ravishankara, 1992; Chu et al., 1993; Huthwelker et al., 2004) and only briefly (if not at all) mention an uptake coefficient γ or an accommodation coefficient α of HCl on ice in the range 0.1 to 0.3. Others have studied the interaction of HCl with ice films in terms of its effects on the morphology (Sadtchenko et al., 2000) and on the disorder and roughness of the substrate surface (McNeill et al., 2007).

Hynes et al. (2001) report γ(HCl) = 0.1 at 205 K with a substantial decrease as the temperature increases with no dependence on P_{HCl} whereas Flückiger et al. (1998) found γ(HCl) in the range from 0.34 to 0.22 in the temperature range 190 to 210 K on pure ice with a negative temperature dependence which has been explained using a two-precursor model (Flückiger and Rossi, 2003). Given the nature of the experiments, namely laminar flow tubes and Knudsen reactors, neither is able to identify the nature of the substrate as they have no means of investigating the condensed phase under the relevant conditions of the uptake experiment. Using a stirred flow reactor similar to the one used in this work, Delval et al. (2003) provided a γ value ranging from 0.05 to 0.01 in the temperature range 200 to 235 K and are able to identify the nature of the substrate by means of FTIR spectroscopy in transmission.

In this work we expand on the results of Delval et al. (2003) by measuring the kinetics of HCl and H_2O interaction on HCl-doped ice substrates whose phase-identity is known, namely HCl hexahydrate or an amorphous HCl/H_2O mixture, in the temperature range 170–205 K. We also discuss the effect of surface disorder on α and we propose a revision of the phase diagram of the binary HCl/H_2O system based on the results obtained for the HCl hexahydrate substrates.

In order to achieve this we have modified and adapted the reactor used by Delval et al. (2003, 2005) and Chiesa and Rossi (2013) as well as described the HCl and H_2O interaction with the reactor walls using a Langmuir adsorption isotherm for both H_2O

ACPD
13, 30765–30839, 2013

and HCl, both separately and in the presence of each other, in order to resolve the difficulties in the quantitative determination of HCl adsorption onto the ice substrate.

2 Experimental apparatus

The results presented in this paper have been obtained using a modified version of a multidiagnostic reactor described elsewhere (Delval et al., 2003). Figure 1 presents a scheme of the modified reactor and Table 1 reports its characteristic parameters. Briefly, the reactor consists of a high vacuum (1×10^{-7} Torr background pressure) stainless steel chamber in which controlled growth of thin ice films in the range 1–2 µm thickness is possible on a temperature-controlled Si substrate. It is equipped with the following diagnostic tools: Pfeiffer Vacuum QMS220 quadrupole Mass Spectrometer (MS), BIORAD FTS-575C FTIR spectrometer equipped with a cryogenic HgCdTe detector and a MKS 627B Baratron absolute pressure gauge. The MS may be equipped with a Prisma™ or a PrismaPlus™ control unit depending on the measurement conditions, as will be explained below. The 1″ diameter Si window, onto which gas condensation takes place, is the only cold surface in the reactor exposed to the admitted gases which allows the establishment of a 1 : 1 correspondence between changes in the gas and the thin film composition. Experimental proof beyond that given previously (Delval et al., 2003; Chiesa and Rossi, 2013) will be given below. The main difference to the reactor described by Delval et al. (2003) is the addition of a GENERAL VALVE CORPORATION Series 9 high speed solenoid valve of 2 mm orifice size controlled by a IOTA ONE driver unit for pulsed gas admission experiments (PV) as well as the introduction of an additional calibrated leak valve in a second bypass line to the MS chamber affording three different gas residence times in the stirred flow reactor (see Table 1). In PV experiments transient supersaturation of gas is obtained by injection of a short pulse of gas molecules of 5–20 ms duration into the reactor. The additional bypass has a larger orifice and enables the extension of the pumping rate range from 0.171 to 0.811 s^{-1} for H_2O at 315 K.

ACPD
13, 30765–30839, 2013

The escape rate constant k_{esc} (s^{-1}) is proportional to the gas molar mass M ($kg\,mol^{-1}$) and the vessel temperature T (K) according to Eq. (1):

$$k_{esc}(T,M) = \sqrt{\frac{8RT}{\pi M}} \cdot \frac{A_{esc}}{4V} = C \cdot \sqrt{\frac{T}{M}} \quad (1)$$

where R is the ideal gas constant in $J\,mol^{-1}\,K^{-1}$, A_{esc} the surface area of the effusion orifice in cm^2, V the reactor volume in cm^3 and C the linear proportionality factor when M is expressed in $g\,mol^{-1}$. k_{esc} has been measured for the three possible combinations of two orifices (small open and large closed, small closed and large open, small and large open) using the effusion of non-reactive gases across both leak valves. For each inert gas used (H_2, He, N_2 and Ar) a calibrated flow of molecules was established which was subsequently halted. The effusion of the gas from the reactor was monitored as a function of time using the MS and resulted in an exponential decay of the signal at the parent mass (m/z = 2, 4, 28 and 40, respectively) whose decay rate was given by the effusion rate constant k_{esc}. The plot of the measured k_{esc} as a function of $\sqrt{T/M}$ provides the scaling factors C for the different orifice combinations, as reported in Table 1, and was used to scale k_{esc} for each gas (M) and temperature (T).

Three different operational conditions may be established: *static*, *dynamic* and *stirred flow*. Under *static* conditions the total pressure inside the reactor is monitored using the MKS Baratron absolute pressure gauge whereas the condensed phase is monitored by means of FTIR spectroscopy in transmission. *Dynamic* conditions are established by opening the 6″ gate valve, thereby reaching the maximum pumping speed of $S = 190\,L\,s^{-1}$ in the reactor, corresponding to $k_{esc}^{Dyn} = 50\,s^{-1}$ for H_2O. Under this condition, a typical flow of $F_i(H_2O) = 1 \times 10^{15}\,molec\,s^{-1}$ of H_2O corresponds to a partial pressure of 2×10^{-7} Torr in the reactor allowing the use of MS to monitor the gas phase whereas the condensed phase is monitored by means of FTIR in transmission. *Stirred flow* (SFR) conditions are established when the gate valve is closed and either one or both calibrated leak valves are open. Under this condition, at a typical flow of

ACPD
13, 30765–30839, 2013

1×10^{15} molec s^{-1} of H_2O, the partial pressure in the reactor chamber varies between 9×10^{-5} to 2×10^{-5} Torr, when the small orifice is open or both leak valves are open, respectively. The gas phase is monitored by means of residual gas mass spectrometry in the lower chamber where the pressure remains lower than 2×10^{-6} Torr at all operating conditions.

The temperature of the Si window is measured by means of a type T (copper/constantan) thermocouple wire clamped into a thermocouple well of the Si window support by a set screw and controlled by a PID program using LabVIEW™. The temperature accuracy in all experiments is ±0.5 K. The temperature of the ice films grown on the Si window may be different from that of the window or support itself. The temperature is therefore calibrated using the vapour pressure of pure ice films measured under static conditions. A pure ice film of approximately 2 µm thickness is grown by backfilling the reactor chamber with the introduction of a calibrated water vapour flow while the window is held at a temperature of approximately 180 K. The system is then set to static condition and the temperature slowly increased within the range 180 to 215 K. The equilibrium vapour pressure of water measured in the reactor as a function of temperature is then compared with literature results (Marti and Mauersberger, 1993). A correction of +2 to 3 K needs to be applied to the measured temperature in order to bring into agreement the equilibrium H_2O vapour pressure and the measured temperature of the Si window. The measured vapour pressure is also corrected to account for the difference in temperature between the ice surface (T_{ice}) and the reactor walls (T_w). Ideally, only T_{ice} of the condensed phase controls the equilibrium vapour pressure P_{eq}, but in practice we work with an experimental system whose walls are at temperature T_w that influences the measured partial pressure. To account for the phenomenon of thermal transpiration (Dushman and Lafferty, 1962), the measured vapour pressure P_{meas} has been corrected throughout this work, whenever it was necessary, according

ACPD
13, 30765–30839, 2013

to Eq. (2):

$$P_{eq} = P_{meas}\sqrt{\frac{T_{ice}}{T_w}} \quad (2)$$

The temperature of the reactor walls is set to a constant value $T_w = 315\,K$, and thereafter we will refer to this temperature as "ambient" temperature.

In order to use the MS as a partial pressure or concentration monitor, a calibration of the MS signal for each gas of interest has been performed. When a gas X is injected into the reactor through the dosing tube at a flow rate $F_i(X)$, measured by means of a pressure drop in a calibrated volume, a mass spectrometric signal I_X is obtained. At steady state, the relation between the flow admitted and the MS signal obtained may be expressed by $F_i(X) = C_X \cdot I_X$ where $F_i(X)$ is the measured flow admitted in molec s^{-1}, I_X is the amplitude of the MS signal in A and C_X the calibration factor for the gas X in molec s^{-1} A^{-1}. The calibration factor C_X may be measured under both dynamic and stirred flow conditions. For all gases used in this work, the calibration factors are identical for both SFR and dynamic conditions, as expected, within a typical experimental error of ±5 %, regardless of the measurement conditions. The calibration factors have been checked frequently throughout the study.

As mentioned above, FTIR spectroscopy in transmission has been used to monitor the condensed phase by collecting spectra averaging 8 scans at a resolution of 4 cm^{-1} in the range 700–4000 cm^{-1}. Typical scan time is 45 to 60 s. FTIR spectroscopy has been used to measure the number of molecules deposited on the Si window if the molecular absorption cross-section is known. From the Beer–Lambert law, the relation for the absorption is as follows:

$$OD = \log\left(\frac{I_0}{I}\right) = 0.4343 \ln\left(\frac{I_0}{I}\right) \quad (3)$$

$$\ln\left(\frac{I_0}{I}\right) = \sigma \cdot n \cdot d \quad (4)$$

ACPD
13, 30765–30839, 2013

where OD is the optical density in absorbance units at a given wavelength and I_0, I are the incident and transmitted intensities at the given wavelength, respectively, σ is the molecular absorption cross section in $cm^2\,molec^{-1}$, n is the concentration in $molec\,cm^{-3}$ and d the optical pathlength in the absorber in cm. Equations (3) and (4) may be combined together to obtain the relation between OD and σ, namely $\ln(10)\cdot OD = \sigma\cdot n\cdot d$.

The volume of the optical sample is given by $V^{FTIR} = d\cdot A_{Si}$, where A_{Si} is the area of the film supported by the Si window ($A_{Si} = 0.99\,cm^2$, one side). Owing to the fact that the total number of molecules deposited on both sides of the Si support, namely N^{FTIR}, may be expressed as $N^{FTIR} = n\cdot V^{FTIR}$, it is then possible to calculate according to Eq. (5):

$$N^{FTIR} = \frac{\ln(10)\cdot OD}{\sigma}\cdot A_{Si} \quad (5)$$

The number of molecules in the solid phase has been used to establish the mass balance of the performed experiments (see below).

In this study three different ice substrates have been used: pure ice films, crystalline $HCl\cdot 6H_2O$ films (HCl hexahydrate, thereafter HH) and amorphous HCl/H_2O mixture films (thereafter amHCl).

The protocol for the growth of pure ice films is as follows: the chamber, under SFR conditions, is backfilled with bidistilled water vapour for a few minutes at flow rates between 5×10^{15}–$10^{16}\,molec\,s^{-1}$, with the Si substrate held at temperatures between 167–175 K. The film grows on both sides on the nominally 1″ Si window to a thickness of typically 1 µm due to the backfilling procedure. The temperature of the support is then set to the desired value at a typical rate of $\pm0.3\,K\,min^{-1}$.

The protocol for the growth of HH films is an extension of the one for pure ice films. After the growth of a pure ice film, the temperature of the Si substrate is held between 165–170 K and the sample is exposed to HCl vapour for roughly 10 min at flow rates between 7×10^{14}–$1\times10^{15}\,molec\,s^{-1}$ at typical vapour pressures P_{HCl} in the range 6 to

ACPD
13, 30765–30839, 2013

8×10^{-6} Torr at SFR conditions and under simultaneous monitoring of HCl at $m/z = 36$. A total dose of approximately 5×10^{17} molecules of HCl is admitted into the reactor. It is important to notice that not all the admitted HCl molecules are adsorbed onto the ice film as roughly 50 % of them are lost either through pumping across the effusion orifice or by adsorption onto the chamber walls. The mass balance for a few selected experiments will be displayed below. The formation of HH on the ice sample is monitored by means of FTIR absorption spectroscopy in transmission as a function of time, both during deposition of HCl and once the admission of HCl has been halted.

The protocol for the growth of amHCl films differs from the HH growth protocol only in the choice of temperature at which the sample is exposed to HCl. After the growth of the pure ice film, the temperature is increased to 175–178 K when a similar dose of HCl compared to HH growth is admitted into the reactor and monitored at $m/z = 36$ (HCl) and $m/z = 18$ (H_2O). Similarly, the formation of amHCl on the thin ice film sample is monitored using FTIR absorption spectroscopy.

3 Experimental methodology

The stirred-flow reactor is characterized by a large internal surface compared to the Si substrate surface (Table 1). Due to the small ratio between these surfaces it is inevitable that atmospheric trace gases admitted during the experiments interact with the stainless steel chamber walls. In order to describe the interaction of H_2O and HCl vapour with the low temperature ice films and the chamber walls the following scheme

ACPD
13, 30765–30839, 2013

has been applied:

$HCl(g) \leftrightarrows HCl(c)$	$k_c(HCl), R_{ev}(HCl)$ (rate of condensation on and rate of evaporation from ice)	(6)
$HCl(g) \rightarrow$ escape	$k_{esc}(HCl)$ (escape rate of HCl across reactor orifice)	(7)
$HCl(ads) \leftrightarrows HCl(g)$	$k_w(HCl), R_w(HCl)$ (rate of adsorption on and rate of desorption from reactor walls)	(8)
$H_2O(g) \leftrightarrows H_2O(c)$	$k_c(H_2O), R_{ev}(H_2O)$ (rate of condensation on and rate of evaporation from ice)	(9)
$H_2O(g) \rightarrow$ escape	$k_{esc}(H_2O)$ (rate of escape of H_2O across reactor orifice)	(10)
$H_2O(ads) \leftrightarrows H_2O(g)$	$k_w(H_2O), R_w(H_2O)$ (rate of adsorption on and rate of desorption from reactor walls)	(11)

where $k_c(HCl)$, $k_c(H_2O)$ are the condensation rate constants on ice in s^{-1} for HCl and H_2O, $R_{ev}(HCl)$, $R_{ev}(H_2O)$ the evaporation rates from the ice in molec s^{-1} cm^{-3}, $k_w(HCl)$, $k_w(H_2O)$ the adsorption rate constants onto the reactor walls, $R_w(HCl)$, $R_w(H_2O)$ the desorption rates from the walls in molec s^{-1} cm^{-3} and $k_{esc}(HCl)$, $k_{esc}(H_2O)$ the effusion rate constants out of the reactor in s^{-1}, respectively.

The aim of this study is to separate the rate of evaporation R_{ev} and the accommodation coefficient α on ice for both gases, HCl and H_2O, in order to obtain the kinetics of evaporation and condensation. Both kinetic parameters are subsequently combined to obtain the corresponding HCl and H_2O equilibrium vapour pressures that may be compared to literature measurements. This approach is known as thermo-chemical ki-

ACPD
13, 30765–30839, 2013

netics where thermodynamic parameters are used as thermodynamic constraints for the measured kinetics.

For a gas X (HCl, H_2O), the following flow balance equation holds in the presence of ice at steady state:

$$F_{in}(X) + F_{des}(X) + F_{ev}(X) = F_{SS}(X) + F_{ads,w}(X) + F_{ads,ice}(X) \quad (12)$$

where all terms are flow rates in molecs^{-1}. In particular, F_{in} is the chosen flow rate of molecules admitted in the reactor, F_{des} the flow rate of molecules desorbing from the reactor walls, F_{ev} the flow rate of molecules evaporating from the ice surface, F_{SS} the flow rate of molecules effusing through the leak valve into the MS chamber, $F_{ads,w}$ the flow rate of molecules adsorbing onto the reactor walls and $F_{ice,w}$ the flow rate of molecules adsorbing onto the ice film.

We assume that the adsorption onto the walls can be described as a Langmuir type adsorption, and under this assumption, Eq. (12) may be expressed as follows (see Appendix A for the mathematical derivation) for a gas X (HCl, H_2O):

$$V \cdot R_{in}(X) + N_{TOT} \cdot k_{des,w}(X) \cdot \theta + V \cdot R_{ev}(X) = \\ = V \cdot R_{SS}(X) + S_w \cdot \frac{\alpha_w(X) \cdot \bar{c}}{4}(1-\theta) \cdot [X] + S_{ice} \cdot \frac{\alpha_{ice}(X) \cdot \bar{c}}{4} \cdot [X] \quad (13)$$

where V is the reactor volume in cm^3, R_{in} the rate of molecules X admitted in the chamber in molecs^{-1} cm^{-3}, N_{TOT} the total number of molecules X adsorbed onto the reactor walls, $k_{des,w}(X)$ the desorption rate constant from the reactor walls in s^{-1}, θ the fractional surface coverage, R_{ev} the rate of evaporation of X from the ice in molecs^{-1} cm^{-3}, R_{SS} the rate of effusion through the leak valve in molecs^{-1} cm^{-3}, S_w and S_{ice} the surfaces of the reactor walls and the ice film in cm^2, α_w and α_{ice} the accommodation coefficients of X on the walls and on the ice film and $\bar{c}$ the mean thermal velocity of a molecule in cm s^{-1}, respectively.

ACPD
13, 30765–30839, 2013

In order to measure the four unknown parameters in Eq. (13), namely $k_{des,w}$, R_{ev}, α_w and α_{ice}, a three-pronged strategy has been adopted: first, pulsed valve experiments with the cryostat at ambient temperature (no ice) have been used in order to measure α_w for HCl and H_2O. Second, the Langmuir adsorption isotherms at ambient temperature for the interaction of HCl and H_2O with the reactor walls in the absence of ice have been measured and $k_{des,w}$ has been obtained. Finally, a combination of pulsed valve and steady state experiments has been used in order to measure α_{ice} and R_{ev}, respectively, for both HCl and H_2O. The details of the different steps follow below.

3.1 Pulsed valve experiments at room temperature

PV experiments are experiments where a transient supersaturation of gas is created in the reactor by admitting a short pulse of molecules in the range 10^{16}–10^{17} molecules per pulse. The admitted dose depends on the stagnant pressure of the reservoir as well as the pulse duration. In order to determine the number of molecules admitted with each pulse the dose dependence has been calibrated using inert N_2 as admitted gas, yielding a typical dose of 5.8×10^{14} molecules per millisecond duration of the pulse per Torr of pressure in the gas reservoir.

With the cryostat at ambient temperature, PV experiments may be used to measure the uptake of HCl and H_2O onto the reactor walls. In the aftermath of a calibrated pulse of known dose, the exponential decay of the mass spectrometer (MS) signal at mass m/z 18 or 36 (k_d) is given by the sum of the measured effusion (k_{esc}) and adsorption rate constant (k_w) on the reactor walls, namely $k_d = k_{esc} + k_w$ (Flückiger et al., 1998).

The measured acquisition frequency of the Prisma™ control unit, expressed has the number of data points recorded per second, is approximately $3\,s^{-1}$, too small to measure decay rate constants in the range 2.5–0.2 s^{-1}. Therefore, in all PV experiments we have used a PrismaPlus™ control unit, which has an acquisition frequency of $250\,s^{-1}$, high enough to measure the rate constants we expect. The dose admitted with each pulse has been calibrated using a non-reactive gas and measuring the total number of molecules admitted in the aftermath of a pulse as a function of the pulse duration and

ACPD
13, 30765–30839, 2013

the reservoir backing pressure by time-integrating the calibrated MS signal that itself was calibrated using a steady-state flow of the same gas coupled to a measurement of the pressure decrease with time in a calibrated volume.

Figure 2 shows an example of pulses admitted into the reactor: The dark blue and red curves correspond to pulses of H_2O and HCl molecules, respectively in the absence of ice. Series of pulses at different doses have been used to determine the accommodation coefficients α_w, which are related to the adsorption rate constants as follows:

$$\alpha_w = \frac{k_w}{\omega} \tag{14}$$

where ω is the calculated gas-surface collision frequency in s^{-1} given in Table 1.

The accommodation coefficient of H_2O on the walls is $\alpha_w(H_2O) = (6.19 \pm 0.08) \times 10^{-6}$ and is roughly 4 orders of magnitude smaller than the measured $\alpha_{ice}(H_2O)$ at temperatures in the range 170 to 200 K, namely $\alpha_{ice}(H_2O) \approx 0.1$ (see below). Since the ratio between the internal wall and the ice surface area is approximately 1000, we consider the internal walls as an active surface that can act as a source or a sink for H_2O vapour, depending on its partial pressure. The contribution of the walls is even more important for HCl: the accommodation coefficient of HCl vapour on the walls is $\alpha_w(HCl) = (1.69 \pm 0.03) \times 10^{-5}$, only a factor of 70 smaller than the lowest value of $\alpha_{ice}(HCl) = 1.2 \times 10^{-3}$ corresponding to the worst case scenario for HCl.

3.2 Langmuir adsorption isotherms for H_2O and HCl on stainless-steel reactor walls at room temperature

In this work, we assumed that the adsorption onto the walls may be described as a Langmuir adsorption. Under this assumption, the coverage of the surface walls θ is a function of the concentration of the gas X (HCl, H_2O) as follows:

$$\theta([X]) = \frac{K_L[X]}{1 + K_L[X]} \tag{15}$$

ACPD
13, 30765–30839, 2013

where K_L ($cm^3\ molec^{-1}$) is the Langmuir constant, which is the equilibrium constant for the adsorption process, namely $K_L = k_c(X)/R_{ev}(X)$, where $k_c(X)$ is the condensation rate constant in s^{-1}. When steady state conditions are established, the concentration of a gas X (X = H_2O, HCl) in the SFR reactor is given by Eq. (16):

$$[X]_{SS} = \frac{F_{SS}(X)}{k_{esc}(X) \cdot V} \quad (16)$$

In order to obtain the coverage θ, we introduce a controlled flow of a gas X into the chamber at SFR conditions and wait for steady state to be established by monitoring the effusion flow using the MS. For non-interactive gases, the time scale to reach steady state conditions is given by the residence time $\tau_r = k_{esc}^{-1}$. Any decrease beyond τ_r has been attributed to the rate of adsorption of gas molecules onto the walls of the reactor, according to $\tau_r = (k_{esc} + k_w)^{-1}$.

Figure 3 shows the results of an experiment performed using HCl vapour: the grey curve represents n-steps of increasing flows of HCl effusing from the reactor as measured by the calibrated MS, corresponding to increasing HCl flows introduced into the reactor chamber. The red shaded area represents the difference between the hypothetical effusion flow $F_{esc,hypo}$, corresponding to a non-interactive case with no adsorption of H_2O or HCl onto the walls, and the measured flow $F_{esc,meas}$ for each j-th time interval. As mentioned above, we attribute this difference to the rate of adsorption of gas molecules onto the reactor walls. Under this assumption, for each time interval j the red shaded area in Fig. 3 is the total number of molecules adsorbed onto the reactor walls, which may be calculated according to Eq. (17):

$$N^j_{ads,w}(X) = \int \left(F_{esc,hypo}(t) - F_{esc,meas}(t)\right) \cdot dt \quad (17)$$

with $F_{esc,hypo}$ and $F_{esc,meas}$ in $molec\,s^{-1}$ and $N^j_{ads,w}(X)$, the cumulative number of molecules adsorbed at each j-th time interval, respectively. The total cumulative number of molecules of gas X adsorbed onto the walls $N^X_{ads,w}$ is the sum of all $N^j_{ads,w}$ and

ACPD
13, 30765–30839, 2013

a function of the steady state concentration of the gas X (HCl, H_2O) and may be expressed in terms of a Langmuir constant as follows:

$$N^{X}_{ads,w}([X]) = \frac{N_{TOT} \cdot K_L[X]}{1 + K_L[X]} \quad (18)$$

where N_{TOT} is the total maximum number of molecules that can be adsorbed on the total internal surface of the SFR vessel. We calculated the coverage as a function of concentration as expressed in Eq. (15) as the ratio between $N^{X}_{ads,w}$ and N_{TOT}:

$$\theta([X]) = \frac{N^{X}_{ads,w}}{N_{TOT}} \quad (19)$$

The experiments were performed under two different conditions:

- *Pure gas system*: only one selected gas was introduced into the reactor (HCl or H_2O)
- *Binary system*: the main gas has been introduced into the reactor together with a constant flow of the other gas in order to simulate the planned experiments at low temperatures.

Figure 4 shows the results for the construction of a Langmuir adsorption isotherm in terms of the wall coverage θ obtained from Eq. (19) for HCl and H_2O interacting with the stainless-steel walls at 315 K as a function of gas concentration according to Eq. (15).

The red circles represent experiments with a pure H_2O flow admitted into the reactor, and the green circles represent experiments where an additional constant flow $F_{IN} = 8 \times 10^{14}$ molec s^{-1} of HCl was introduced into the reactor together with the variable H_2O flow.

The black triangles represent the interaction of pure HCl, the blue triangles the interaction of HCl in the presence of an additional H_2O flow admitted into the reactor.

ACPD
13, 30765–30839, 2013

For HCl we adopted a similar approach but the results are different: in the presence of additional H_2O flow, the HCl coverage is lower, in contrast to the previous case. In the following discussion we will provide an interpretation for this difference.

N_{TOT} represents the total maximum number of molecules that can be adsorbed onto the stainless-steel surface. For H_2O, in the presence of HCl, it corresponds to $N_{MAX} = 4.45 \times 10^{14}$ molec cm^{-2}, approximately 45 % of a formal monolayer coverage of H_2O on ice (1 ML(H_2O) = 1×10^{15} molec cm^{-2}), whereas for pure HCl it corresponds to $N_{MAX} = 2.68 \times 10^{14}$ molec cm^{-2}.

The number of molecules in a formal monolayer (ML) of HCl may be estimated from bulk densities using the expression $ML = (\rho N_A/M)^{2/3}$, where ρ, N_A and M are the bulk density, Avogadro's number and molar mass, respectively. The density $\rho = 1.490$ kg L^{-1} for pure liquid HCl at $T = -85$ °C (CRC Handbook) yields a value for one ML of 8.53×10^{14} molec cm^{-2}. The Matheson Gas Data Book provides a density of $\rho = 0.879$ kg L^{-1} for liquid HCl at $T = 10$ °C and $P = 32$ atm, from which a value for one ML of 6.0×10^{14} molec cm^{-2} may be calculated. This last value has been used in the present work given the temperature of the reactor internal surfaces ($T_w = 42$ °C) comparable to the entry given in the Matheson Gas Data Book. The maximum HCl coverage in the present system ($N_{MAX} = 2.68 \times 10^{14}$ molec cm^{-2}) obtained from the Langmuir isotherm at saturation corresponds therefore to approximately 45 % of a formal monolayer coverage of HCl on stainless steel. We also report that on ice, a formal monolayer of HCl has been measured by Henson et al. (2004) to be 2.3×10^{14} molec cm^{-2} using BET analysis, which compares well with our measurement of N_{MAX} and points to a coverage of approximately 1 formal monolayer of HCl on the system internal surfaces on the basis of 2.3×10^{14} molec cm^{-2} of HCl for a monolayer coverage on ice. However, the consensus value for HCl coverage on an ice film is closer to 2.7×10^{14} molec cm^{-2} (Chiesa and Rossi, 2013).

For a gas X, the Langmuir equilibrium constant is a function of the accommodation coefficient $\alpha_w(X)$ and the desorption rate constant $k_{des,w}(X)$ (s^{-1}) according to Eq. (20)

ACPD
13, 30765–30839, 2013

(see Appendix A, Eq. A6):

$$K_L = \frac{S_w \cdot \alpha_w(X) \cdot \bar{c}/4}{N_{TOT} \cdot k_{des,w}(X)} \quad (20)$$

where S_w is the internal surface in cm^2 and N_{TOT} the total number of adsorption sites on the surface. The fitting parameters of the Langmuir isotherms provide K_L and N_{TOT} for the present experimental system whereas $\alpha_w(X)$ has been measured directly from a real-time observation as reported in Sect. 3.1 thus allowing the calculation of $k_{des,w}$.

3.3 Pulsed valve and steady state experiments at low temperatures

A combination of pulsed valve and steady state experiments has been used to measure α_{ice} and R_{ev}, respectively, for both HCl and H_2O interacting with the thin ice film. After the growth of the selected substrate according to the protocols reported above, the thin film is set to a chosen temperature. When steady state conditions are established, a series of three gas (HCl, H_2O) pulses at intervals of approximately 60 s is admitted into the reactor. Similarly to PV at room temperature, the exponential decay of the MS signal at m/z 18 or 36 (k_d) is given by the sum of the measured k_{esc}, the adsorption rate constant on the walls (k_w) and the adsorption rate constant (k_{ice}) onto the ice, namely $k_d = k_{esc} + k_w + k_{ice}$, in the aftermath of a pulse. We then calculate the accommodation coefficient $\alpha_{ice}(X)$ of a gas X (X = HCl, H_2O) onto the ice substrates according to Eq. (21):

$$\alpha_{ice} = \frac{k_{ice}}{\omega} \quad (21)$$

The steady state MS signal established before the pulse series represents the flow rate of molecules effusing through the leak valve $F_{SS}(X)$ in Eq. (12) and it may be used to calculate $R_{ev}(X)$ from Eq. (13). Figure 5 shows an example of the combined PV and steady state experiments for H_2O pulses as a function of time on a HH substrate

ACPD
13, 30765–30839, 2013

taking note of the large disparity of the MS signal for HCl and H_2O. H_2O flow rate with a series of pulses at temperatures of 176 and 181.5 K is shown in blue on the right axis. The red curve on the left axis represents the corresponding HCl flow rate at the same temperatures. At 176 K, the correspondent flow rates of H_2O and HCl are measured. Subsequently, for technical reasons, only the H_2O signal at m/z 18 is recorded and a series of three H_2O pulses is admitted into the reactor. From the pulse decay rate k_d, $\alpha_{ice}(H_2O)$ may be calculated according to Eq. (21). As the temperature is increased to 181.5 K, both masses m/z 18 and 36 are again recorded. When steady state is established for the new target temperature, a new series of H_2O pulses is admitted. The steady state flow before the pulse series represents $F_{SS}(H_2O)$ in Eq. (12) and it may be used to calculate $R_{ev}(H_2O)$ from Eq. (13). This protocol has been applied using HH and amHCl as substrates as well as alternating H_2O and HCl as probing gases using a series of pulses at temperatures in the range 167 to 203 K. The orange curve in Fig. 2 shows an example of HCl pulses over ice, compared to a pulse (red curve) in the absence of ice.

With the separation of R_{ev} and α_{ice} for both HCl and H_2O, we may calculate the equilibrium vapour pressure $P_{eq}(X)$ for each gas, corrected according to Eq. (2), as follows:

$$P_{eq}(X) = \frac{R_{ev}(X)}{k_c(X)} \cdot \frac{RT}{N_A} \quad (22)$$

where R is the molar gas constant in $cm^3\,Torr\,K^{-1}\,mol^{-1}$, T the temperature of the thin film in K and N_A the Avogadro constant in $molec\,mol^{-1}$. In our current setup only one gas at a time can be used for PV experiments. When the ice film is exposed to a transient supersaturation of H_2O and $\alpha_{ice}(H_2O)$ and $F_{SS}(H_2O)$ are measured, we may calculate $P_{eq}(H_2O)$ whereas only F_{SS}(HCl) can be measured, as shown in Fig. 5.

The flow F_{SS}(HCl) may still be used to calculate P_{eq}(HCl) in H_2O-PV experiments when coupled with α_{ice}(HCl) measured in HCl-PV experiments according to Eqs. (13) and (22).

ACPD
13, 30765–30839, 2013

Similarly, when the ice film is exposed to a HCl pulse both $\alpha_{ice}(HCl)$ and $F_{SS}(HCl)$ are measured in order to calculate $P_{eq}(HCl)$ and only $F_{SS}(H_2O)$ is obtained. $F_{SS}(H_2O)$ is then coupled with $\alpha_{ice}(H_2O)$ from H_2O-PV experiments in order to calculate $P_{eq}(H_2O)$ in HCl-PV experiments.

4 Results

In the following section the results obtained applying the method described above will be presented. As mentioned before, once the selected substrate, amHCl or HH, has been grown according to the corresponding protocol, the film is set to a chosen temperature. When steady state conditions are established, the corresponding flows $F_{SS}(H_2O)$ and $F_{SS}(HCl)$ are recorded. Subsequently the series of gas X (HCl, H_2O) pulses are admitted into the reactor, from which $\alpha_{ice}(X)$ may be calculated according to Eq. (21). The film is then set to a higher temperature, $F_{SS}(H_2O)$ and $F_{SS}(HCl)$ are recorded and the series of pulses repeated on the same ice sample. The cumulative dose on the ice sample has been measured as the difference between the admitted dose and the number of molecules effused from the reactor in the aftermath of each pulse. This experimental protocol has been repeated for each measured point in the temperature interval of interest and repeated for both series of gases, HCl and H_2O, pulses.

4.1 Amorphous HCl/H_2O mixture thin films

The results for amHCl are reported in Fig. 6. Panel c shows the measured $\alpha_{ice}(X)$, X = (H_2O, HCl), as a function of temperature. $\alpha_{ice}(H_2O)$ on pure ice (inverse blue triangles) varies from 0.12 at 175 K to 0.054 at 203 K. $\alpha_{ice}(H_2O)$ on amHCl (red circles) decreases as a function of temperature, being equal to $\alpha_{ice}(H_2O)$ on pure ice within experimental error in the range 175–185 K and lower by approximately 20 % at temperatures higher than 185 K. Coloured triangles represent results for $\alpha_{ice}(HCl)$ on amHCl, where the colour scale gives the accumulated dose of HCl on the HCl-doped ice film

ACPD
13, 30765–30839, 2013

after each pulse. α_{ice}(HCl) is equal within experimental error to α_{ice}(H_2O) on pure ice up to 180 K and lower by a factor of approximately 2 above 180 K. Consistent with the experimental protocol, the ice samples are increasingly enriched in HCl as the temperature increases. Fresh ice samples have been exposed to HCl pulses at temperatures of 194 and 200 K and α_{ice}(HCl) is higher by a factor of 1.5 and 1.25 compared to aged samples, respectively. This result compares favourably with the observation of Flückiger et al. (1998) who have noticed a dose dependence of the kinetics of HCl adsorption on pure ice exposed to transient supersaturation.

Panel b shows results for R_{ev} in molec s^{-1} cm^{-3} as a function of temperature. Inverse blue triangles represent pure ice, red circles H_2O and black triangles HCl results, respectively. R_{ev}(HCl) is significantly different, lower by a factor of 10 in the temperature range 175–185 K and lower by up to a factor of 100 at temperatures higher than 185 K compared to R_{ev}(H_2O) which is equal to R_{ev}(H_2O) of pure ice across the temperature range 175–205 K. This result further confirms the finding of Delval et al. (2003) that the evaporation of H_2O, despite the presence of adsorbed HCl onto the ice substrate, takes place at a rate characteristic of pure ice in a H_2O-enriched substrate, that is at a low HCl content of the condensed phase. The full green line shows the rate of evaporation of pure water for the system in use calculated from literature results of equilibrium vapour pressure (Marti and Mauersberger, 1993) using $\alpha = 1$, whereas the dashed green line represents extrapolated values of R_{ev}(H_2O) for temperatures lower than 173 K using the expression provided by Marti and Mauersberger.

Panel a shows the results for P_{eq} in Torr calculated according to Eq. (22) for both H_2O and HCl. The same symbols as in panel b are used. P_{eq}(HCl) of amHCl is lower by a factor of 100 at temperatures higher than 185 K compared to P_{eq}(H_2O) of amHCl which is equal within experimental uncertainty to P_{eq}(H_2O) of pure ice. At temperatures lower than 185 K P_{eq}(HCl) of amHCl is still lower than P_{eq}(H_2O) of amHCl but only by a factor of 10, less so than at higher temperatures. The solid green line represents the vapour pressure of water according to the results of Marti and Mauersberger (1993).

ACPD
13, 30765–30839, 2013

The dashed green line represents extrapolated values of $P_{eq}(H_2O)$ for temperatures lower than 173 K.

The values obtained for the equilibrium vapour pressure have been compared with the HCl/H_2O phase diagram constructed by Molina and coworkers (Abbatt, 1992; Molina, 1994; Wooldridge, 1995). Figure 7 shows the results for amHCl films, which all lie within the existence area of HH. This is expected since the dose admitted into the reactor chamber is the same used during the HH growth protocol, namely 5×10^{17} molecules of HCl compared to approximately 4×10^{18} molecules of H_2O, corresponding to an average mole fraction $\chi_{HCl} = 0.111$.

4.2 Crystalline hexahydrate films

The results for HH are reported in Fig. 8. Panel c shows the measured $\alpha_{ice}(X)$ as a function of temperature. Inverse blue triangles represent $\alpha_{ice}(H_2O)$ on pure ice, as shown in Fig. 6. $\alpha_{ice}(H_2O)$ on HH (red circles) decreases a function of temperature and is lower by a factor of approximately 1.5 than $\alpha_{ice}(H_2O)$ on pure ice at temperatures higher than 185 K. Coloured triangles represent results for α_{ice}(HCl) on HH, with the colour scale showing the increasing accumulated dose of HCl on the HCl-doped ice film. α_{ice}(HCl) shows larger scatter compared to amHCl with a variation up to a factor of 10 for results at the same temperature across the full temperature range. Furthermore, each series of three pulses spaced by typically 60 to 90 s always showed a decrease in α_{ice}(HCl) between the first and the last pulse. Similar results have been shown previously in the literature (McNeill et al., 2007) where the scatter has been explained in terms of the morphology or the smoothness of the ice surface. We will discuss these results further in the discussion section.

Panel b shows results for the R_{ev} in molecs^{-1} cm^{-3} as a function of temperature. R_{ev}(HCl) on HH, represented by black triangles, is lower by a factor of 100 across the temperature range 165–193 K compared to $R_{ev}(H_2O)$ on HH which, being equal to $R_{ev}(H_2O)$ on pure ice within experimental error, indicates that the presence of crys-

ACPD
13, 30765–30839, 2013

talline HH on the ice substrate does not substantially affect the evaporation of H_2O which is that of pure ice, in a manner similar to amHCl as described before.

Panel a shows the results for P_{eq} in Torr calculated according to Eq. (22) for both H_2O and HCl. $P_{eq}(H_2O)$ of HH is equal to $P_{eq}(H_2O)$ of pure ice within experimental error whereas P_{eq}(HCl) of HH is lower by a factor of 4 to 15 compared to $P_{eq}(H_2O)$ of HH. The scatter of P_{eq}(HCl), being of the same magnitude as the scatter of α_{ice}(HCl), may likewise be explained by a variation in the substrate composition as well as by an increase in its roughness or inhomogeneous nature due to the exposure to HCl pulses.

Figure 9 shows the phase diagram of the results obtained for HH films: most of the results lie in the HH existence region, as expected, but there is a significant number of points lying outside the HH existence area. In order to determine whether or not this result pertains to the hexahydrate phase we took advantage of the multidiagnostic capabilities of the apparatus and focused our attention to the condensed phase using the corresponding FTIR spectrum for each of the experiments in question.

4.3 FTIR spectra of hexahydrate

The FTIR spectrum of hexahydrate is known from the literature (Ritzhaupt and Devlin, 1991; Koehler et al., 1993; Toon et al., 1994; Graham and Roberts, 1997). For each point in Fig. 9, a corresponding spectrum of the thin film has been collected. All spectra corresponding to experiments lying in the HH existence region are a mixture of pure ice and HH film as they have the spectroscopic signature of hexahydrate phase, namely the two additional peaks in the OH stretching region at 3426 and 3366 cm^{-1} and the sharp peak at 1635 cm^{-1}, corresponding to the bending vibration of the proton ordered waters of hydration. Likewise, the spectra corresponding to experiments lying outside the known published HH existence region appear to be a combination of pure ice and pure HH. In order to clearly indicate the presence of HH as well as the HH : ice mixing ratio for these experiments we deconvoluted all experimental spectra. We assume that the measured composite spectrum is a superposition of the spectra of pure ice and pure HH, and we proceeded as follows in order to deconvolute the absorption spec-

ACPD
13, 30765–30839, 2013

trum: the sharp IR peak at 1635 cm^{-1} is an unambiguous marker of HH. Therefore, the optical density at this peak can be used as a marker of the amount of HH present in the ice film. We scaled the optical density at 1635 cm^{-1} of an independently recorded spectrum of pure HH to that of the spectrum of interest. The scaled spectrum is that of the pure HH component and we obtain the pure ice component from the measured composite spectrum after subtraction.

Figure 10 shows an example of the deconvolution: the green spectrum is the recorded spectrum, that is the superposition of pure HH and pure H_2O-ice, the red spectrum is the measured spectrum of pure HH scaled to the measured amplitude of the IR absorption peak at 1635 cm^{-1} and the blue spectrum corresponds to the difference of the green and the red spectrum. It is obvious that the measured spectrum is that of a film where pure ice and pure HH coexist. The procedure does not take into account possible small shifts of up to ±2 cm^{-1} of the pure component spectrum in the presence of the other component, in agreement with the wavelength accuracy of the FTIR spectrometer in the current configuration.

Figure 11 shows the HCl/H_2O phase diagram and the FTIR spectra of a few experiments outside the known HH existence area, labelled accordingly. Each spectrum panel shows the measured FTIR spectrum in the same colour as the vapour pressure plotted in the bottom left panel as well as its deconvolution into a pure ice component (blue spectrum) and a pure HH component (red spectrum). This procedure has been applied to all experiments outside the known HH existence area. For all cases the same conclusion has been reached, namely that all measured $P_{eq}(HCl)$ results in Fig. 9 are indeed pertaining to binary HH/ice films of various composition.

ACPD
13, 30765–30839, 2013

5 Discussion

5.1 Langmuir adsorption isotherms

In order to describe the adsorption of HCl and H_2O onto the reactor internal surface we used Langmuir adsorption isotherms to fit the experimental measurements of HCl and H_2O surface coverage. As shown in Fig. 4, the presence of a HCl flow during H_2O steady state experiments (green circles) presumably enhances the capability of H_2O to adsorb onto the walls, whereas the presence of an additional H_2O flow during HCl exposure reduces the HCl coverage. This may be due to the fact that H_2O and HCl are adsorbed onto different adsorption sites in single gas experiments, but in the presence of a HCl flow the H_2O may also adsorb onto HCl occupied sites, perhaps owing to the high solubility of HCl in H_2O at large H_2O surface coverage. The system, on the other hand, is not symmetric and HCl may be more site-selective compared to H_2O. Therefore, the presence of an additional H_2O flow reduces the number of available sites for HCl adsorption and thus the internal wall coverage of HCl.

Another reason for the decrease of HCl coverage in the presence of H_2O may be the so called common ion effect, induced by the presence of two NaCl salt windows of 20 cm^2 surface (2″ diameter): the sodium chloride on the salt windows is dissociated by water into Na^+ and Cl^- ions. The common Cl^- ion reduces the solubility of HCl thus limiting the coverage on the walls. This effect may help reduce the coverage of HCl, but due to the limited surface of the NaCl windows (40 cm^2) compared to the total internal surface (1885 cm^2) it is unlikely to explain the reduction of K_L by approximately a factor of 7 shown in Fig. 4.

Langmuir isotherms are not the only isotherms used to describe surface adsorption. For instance, Deitz and Turner (1970) used conventional Type II physical adsorption isotherms to describe the adsorption of water on the walls of a glass-Kovar stainless steel vacuum system in the pressure range from 0.2 to 5 Torr. They conclude that the water adsorption strongly depends on the materials and needs to be determined for each apparatus. On the other hand, electrochemical quartz crystal measurements have

ACPD
13, 30765–30839, 2013

been used to determine the adsorption of fission products (caesium and iodide) in their ionic form on the surface of stainless steel and zirconium (Répánszki et al., 2007). The authors conclude that a Langmuir type isotherm can describe the adsorption, where the saturation values correspond to surface monolayers.

Furthermore, Langmuir adsorption models have also been used to successfully describe sub-monolayer adsorption of organic compounds on ice (Winkler et al., 2002; von Hessberg et al., 2008) as well as inorganic compounds on ice (Pouvesle et al., 2010).

5.2 Mass balance and stoichiometry

When introduced into the SFR at low temperatures in the presence of ice, a molecule of X may follow one of three different paths: it may effuse out of the reactor through the leak valve, it may be adsorbed onto the walls of the reactor or it may condense onto the low temperature ice. Namely, if N_{in} is the number of molecules introduced into the reactor, we have $N_{in} = N_{esc} + N_{ads} + N^{FTIR}$, where N_{esc} is the number of molecules that effuse out of the chamber, N_{ads} the molecules adsorbed onto the internal walls of the reactor, calculated according to Eq. (18), and N^{FTIR} is the number of molecules in the condensed ice phase.

N_{in} is measured by means of a pressure drop in a calibrated volume, N_{esc} corresponds to the integral over time of the calibrated MS signal and N_{ads} may be calculated according to Eq. (18) using the measured equilibrium constant K_L.

We calculate N^{FTIR} in the case of HCl as follows: using the measured optical density at 1635 cm^{-1} and the known IR cross section at the same frequency, $\sigma = (6.5 \pm 1.9) \times 10^{-19}$ cm^2 (Chiesa and Rossi, 2013), the number of HCl molecules in the condensed phase may be calculated according to Eq. (23):

$$N^{FTIR}_{HCl} = \frac{\ln(10) \cdot OD^{1635}}{\sigma} \cdot A_{Si} \quad (23)$$

ACPD
13, 30765–30839, 2013

where OD is the optical density in absorbance units, A_{Si} is the area (one side) of the silicon film support and σ is the IR absorption cross section at 1635 cm^{-1}, respectively. Making use of the multidiagnostic capabilities of the system we may therefore calculate a mass balance ratio between the molecules in the gas phase and the molecules in the condensed phase as $(N_{in} - N_{esc} - N_{ads})/N^{FTIR}$.

The number of molecules of H_2O in the condensed phase may be calculated similarly according to Eq. (24):

$$N_{H_2O}^{FTIR} = \frac{\ln(10) \cdot OD^{3233}}{\sigma} \cdot A_{Si} \quad (24)$$

where $\sigma = (8.0 \pm 0.8) \times 10^{-19}$ cm^2 (Chiesa and Rossi, 2013) is the IR absorption cross section of pure ice at 3233 cm^{-1}.

Equations (23) and (24) may be used to determine the stoichiometry of the condensed phase. Upon formation of HH during exposure of HCl the peak intensity at 3233 cm^{-1} decreases. The decrease in OD may be used to calculate the number of H_2O molecules that are used to construct the new crystalline $HCl \cdot 6H_2O$ phase. The number of available H_2O is given by the total number of H_2O in the pure ice film before HCl exposure and calculated according to Eq. (24). When the HCl exposure to the ice film has been halted, the deconvolution procedure described in Sect. 4.3 has been applied to the spectrum of the film at steady state conditions. The resulting spectrum for the excess water (blue spectrum in Fig. 10) is then used to calculate the number of pure H_2O in the sample not associated with HCl, according to Eq. (24). The number of HCl molecules in the sample, namely $N^{HH}(HCl)$, is calculated according to Eq. (23).

The difference between the H_2O molecules in the starting pure ice film and the pure H_2O in the doped sample after suitable deconvolution leads to the number of H_2O molecules that have been used to construct the HH phase, namely $N^{HH}(H_2O)$. Finally, the ratio $N^{HH}(H_2O)/N^{HH}(HCl)$ reveals the stoichiometry of the crystalline film which is $H_2O : HCl = 6 : 1$ according to column 7 of Table 3 if we exclude an outlier.

ACPD
13, 30765–30839, 2013

Table 3 shows results for all experiments reported performed. In all cases the mass balance ratio and the stoichiometry of the condensed phase have been calculated at the end of the HH growth protocol, once steady state conditions had been reached and before PV experiments began. The mass balance ratio yields an average value of 1.182 ± 0.123. The wall-adsorbed molecules account for about 12 to 19 % of the total number of molecules let into the reactor and for about 22 to 30 % of the number of molecules adsorbed onto the ice. These results show that particular caution has to be paid to the description of the gas-wall interaction in the SFR due to the importance it has in the processes involved. The calculated stoichiometry yields an average value of 5.82 ± 0.79, comparable to the theoretical value of 6 for $HCl \cdot 6H_2O$. If we regard experiment 4 as an outlier because it is barely inside the 2σ interval, we obtain an average value for the stoichiometry of the crystalline phase of 6.16 ± 0.29, remarkably close to the expected theoretical value considering the experimental uncertainty.

5.3 HCl/H_2O phase diagram

As described in Sect. 4.3, the deconvolution procedure shown in Fig. 11 leads to observable HCl hexahydrate concentrations for all experiments conducted outside the known HH existence area. They all pertain to binary HH/ice films and we, therefore, propose to extend the existence area of $HCl \cdot 6H_2O$ by modifying the HCl/H_2O phase diagram to include the present results, as shown in Fig. 12 by the shaded area. We preserve the slope of the coexistence line of hexahydrate and trihydrate as calculated by Wooldridge et al. (1995) and simply apply a parallel displacement of the phase boundary whose slope depends on the stoichiometry of the two hydrates and their enthalpies of sublimation.

Figure 13a shows the phase diagram as a function of the equilibrium vapour pressures $P_{eq}(H_2O)$ and $P_{eq}(HCl)$, reconstructed from Hanson and Mauersberger (1990). The empty triangles represent the calculated values of $P_{eq}(H_2O)$ and $P_{eq}(HCl)$ for HH using the kinetic results for adsorption and desorption obtained from the present work, according to Eq. (22). The proposed extension of the HH existence area is represented

ACPD
13, 30765–30839, 2013

as well. The quadruple points remain and are not affected by the additional data. Figure 13b shows an example of two experiments as a time-series when the temperature of the ice substrate is increased in the range 167 to 197 K. Both experiments have been performed as described in Sect. 3.3.

Before describing the two experiments represented by red and purple lines, it is important to understand the behaviour of a sample in a simpler case. We will follow the black dotted line labelled "180 K" in panel a, which represents the isotherm at temperature $T = 180$ K. Along this line, $P_{eq}(HCl)$ may be increased up to approximately 2.5×10^{-7} Torr with almost no detectable change in $P_{eq}(H_2O)$. The sample behaves as pure ice even in the presence of small amounts of HCl. When the phase boundary line is reached, the phase changes from "ice" to HH. Any further increase of $P_{eq}(HCl)$ corresponds to a decrease of $P_{eq}(H_2O)$ as expected for a binary system at equilibrium following the law of Gibbs–Duhem, Eq. (25):

$$d\mu_{HCl} = -\frac{n_{H_2O}}{n_{HCl}} \cdot d\mu_{H_2O} \quad (25)$$

where n_{HCl} and n_{H_2O} are the number of moles of HCl and H_2O and $d\mu_{HCl}$ and $d\mu_{H_2O}$ the change in chemical potential, respectively. A variation in the chemical potential of a component (HCl) in the condensed phase corresponds to the inverse variation of the chemical potential of the other component (H_2O) in proportion to the stoichiometric ratio of the two components. A large variation of $P_{eq}(HCl)$ is allowed along an isotherm compared to a much smaller variation of $P_{eq}(H_2O)$.

As HCl increases along the isotherm, $P_{eq}(H_2O)$ decreases until the boundary line between hexahydrate and trihydrate is reached and the phase changes again. The slope is less steep, reflecting the change of stoichiometry in the new solid phase. A change in temperature leads to deviations from this simple case and the substrate may follow different paths to reach equilibrium. The experiments shown as red and purple lines in panel b describe the evolution of the substrate when the partial pressure of water is controlled by the introduction of an external H_2O flow $F_{in}(H_2O)$ into the reactor.

ACPD
13, 30765–30839, 2013

First we will discuss the experiment marked in red symbols in Fig. 13b. Point 1 is the first measurement taken at 171 K, subsequently the temperature is increased to point 2 (175 K) while no external flow of H_2O is introduced. Nevertheless, a substantial decrease in $P_{eq}(HCl)$ is observed, not only during this particular experiment, but for all experiments reported in panel a. As explained above, a decrease in $P_{eq}(HCl)$ corresponds to an increase of $P_{eq}(H_2O)$, which implies the presence of a flow of H_2O. The water is introduced into the reactor involuntarily across numerous small leaks owing to the presence of elastomeric seals (Viton O-rings) which add up so as to become non-negligible at these low partial pressures of H_2O. Consistent with this fact is our observation of an increase of the thickness of the ice film due to deposition of H_2O onto the ice at temperatures lower than 175 K.

From point 2 to point 3 (180 K) the temperature is increased and only a small increase in $P_{eq}(H_2O)$ is observed compared to a large increase of $P_{eq}(HCl)$. Between point 3 to point 4 $F_{in}(H_2O)$ is introduced into the reactor at constant temperature. As a consequence $P_{eq}(HCl)$ decreases along the isotherm following the increase of $P_{eq}(H_2O)$ as expected according to Gibbs–Duhem, Eq. (25). Both the temperature and $F_{in}(H_2O)$ are increased from point 4 to point 7 such that $F_{in}(H_2O)$ is kept approximately at $0.1 \cdot F_{ev}(H_2O)$ at any temperature. After the measurement at point 7, $F_{in}(H_2O)$ is halted and the system immediately responds to the variation of $P_{eq}(H_2O)$ by increasing $P_{eq}(HCl)$ following the isotherm at $T = 190$ K, according to Gibbs–Duhem, Eq. (25).

The experiment marked in purple symbols in Fig. 13b is performed in a similar way as above (red symbols) with the difference that the external flow $F_{in}(H_2O)$ is a factor of 2 lower with respect to the "red" experiment. From point 1 to point 2 we observe a drop in $P_{eq}(HCl)$ due to background H_2O flow and at point 6 $F_{in}(H_2O)$ is introduced into the reactor. A lower $F_{in}(H_2O)$ leads to higher $P_{eq}(HCl)$ compared to the "red" experiment as is evident from points 7, 8 and 9 that explore the hitherto unexplored space of the HCl hexahydrate phase diagram marked as shaded area in Fig. 13. At point 10 the flow $F_{in}(H_2O)$ is increased to approximately $0.2 \cdot F_{ev}(H_2O)$ with a corresponding increase

ACPD
13, 30765–30839, 2013

of $P_{eq}(H_2O)$ and decrease of $P_{eq}(HCl)$ along the isotherm, once again according to Gibbs–Duhem, Eq. (25).

5.4 α(HCl) scatter and HCl hexahydrate composition

Figure 8 shows the kinetic results for HH substrate experiments. Variations in the kinetic and thermodynamic parameters up to a factor of 10 for points at the same temperatures occur. The substrate is a binary system composed of a bulk pure ice film with a thinner HH film on top of it. According to Gibbs' phase rule, we have $F = C - P + 2 = 2 - 3 + 2 = 1$, where F is the number of degrees of freedom, C the number of components, namely H_2O and HCl, and P the number of phases of the system at equilibrium, namely the binary condensate, the pure ice and the gas phase. The degree of freedom of our system corresponds to the composition of the substrate, namely the mole ratio between pure ice and the HH film. Even though the growth protocol has been applied consistently to all experiments, the approach to the temperatures of interest and the exposure to transient supersaturation of gases during PV experiments which all contribute to the "history" of the film, may lead to a different composition of the thin film at the same experimental temperature which may explain, at least in part, the scatter of $\alpha_{ice}(HCl)$ as a function of temperature. The decrease of $\alpha_{ice}(HCl)$ in the aftermath of a pulse may also be explained as a variation of the composition of the interface, specifically a variation from a H_2O-rich ice film before the first pulse of HCl to a more H_2O-deficient ice film when the third HCl pulse is admitted due to evaporation of H_2O and accumulation of HCl.

$\alpha_{ice}(H_2O)$ on the other hand, does not present any scatter and this may be due to the fact that the average molecular environment for H_2O is constant owing to its single-component nature: H_2O PV experiments always increase the concentration of H_2O in the film, leading to pure ice behaviour.

In order to evaluate the ratio between pure HH and pure H_2O ice we have made use of the multidiagnostic capabilities of the present system. We have selected experiments in five temperature ranges, and for each experiment we have determined the number of

ACPD
13, 30765–30839, 2013

HH molecules using Eq. (23), and similarly the number of molecules of H_2O according to Eq. (24).

The mole fraction χ_{H_2O} of H_2O in each HH film may be calculated as the ratio of the number of moles of H_2O molecules to the total number of moles, namely:

$$\chi_{H_2O} = \frac{N_{H_2O}^{FTIR}}{N_{H_2O}^{FTIR} + N_{HCl}^{FTIR}} \quad (26)$$

Figure 14 shows the results obtained for the selected experiments. P_{eq}(HCl) is reported as coloured circles whereas α(HCl) is presented as coloured triangles according to the temperature range. Temperature seems to have only a modest effect on the composition whereas the history of the sample seems to have a larger impact on the film composition of every individual sample.

P_{eq}(HCl) increases as the concentration of HCl in the film increases, as expected, according to the change in chemical potential in the binary system. α(HCl) decreases as excess H_2O evaporates and the concentration of HCl increases accordingly because the faster H_2O evaporation compared to HCl leads to a situation where less and less water is available in the condensate to accommodate the HCl molecules in the gas phase that hit the ice surface. The presence of the common ion Cl^- in the condensed phase further slows down HCl adsorption, thus reducing α(HCl).

At high HCl concentration and OD at 3233 cm^{-1} lower than 0.15 adsorbance units, that is when the film thickness is less than 0.15 µm, we observe a decrease of $R_{ev}(H_2O)$ as well as an increase of R_{ev}(HCl) in agreement with Chiesa and Rossi (2013) and Delval et al. (2003). This is an indication of a phase change, namely the conversion of HH into an amorphous mixture of higher HCl : H_2O ratio.

Nevertheless, the composition of the HH film cannot completely explain the scatter in the values of α(HCl) and P_{eq}(HCl) such as displayed in Fig. 8. McNeill et al. (2007) have observed variations up to a factor of 3 for the HCl partial pressure of smooth ice samples exposed to HCl vapour after HH formation and they have explained these

ACPD
13, 30765–30839, 2013

variations in terms of the surface roughness and surface disorder of the ice substrates. The scatter in our results may also be due in part to surface morphology variations or inhomogeneities of the film surface of each sample. The ice sample is repeatedly exposed to a high supersaturation of HCl during PV experiments and this may lead to surface liquefaction and/or reconstruction coupled to concentration changes of the surface components compared to bulk composition.

5.5 Composition of amorphous phase

In order to provide an estimate of the composition of the amHCl substrates we compared the present spectra with the ones from Xueref and Dominé (2003). In their work the authors grew doped ice films by co-condensation of gaseous mixtures HCl : H_2O of 5 : 1, 1 : 10, 1 : 50 and 1 : 200 composition at 190 K. The condensation of the 5 : 1 mixture leads to a solid that resembles $HCl \cdot 2H_2O$ where partial crystallization takes place, whereas the condensation of gaseous mixtures of HCl: H_2O ratios of 1 : 10, 1 : 50 and 1 : 200 leads to the formation of non-crystalline solids whenever there is excess H_2O. In particular, the 1 : 10 gaseous mixture leads to a solid of composition in the range 1 : 2 to 1 : 4 regarding HCl : H_2O, while the 1 : 50 and 1 : 200 gaseous mixtures both lead to solids of composition in the range 1 : 4 to 1 : 6.

The authors reason that due to the excess in HCl incorporation in the co-condensation process, H_2O and HCl are not in thermodynamic equilibrium. This may lead to the formation of a supersaturated homogenous solid solution of HCl in ice, the formation of a heterogeneous solid made of crystalline hydrates and a solid solution of HCl in ice and/or the diffusion to the surface of the excess HCl and its subsequent escape into the gas phase, bringing the solution into thermodynamic equilibrium. Xueref and Dominé invoke the slightly larger HCl/ice accommodation coefficient α(HCl) compared to $\alpha(H_2O)$ on pure ice as the reason of HCl enrichment in the condensed phase. While this goes into the right direction we think that this explanation is by far insufficient to rationalize the large observed enrichment factors in laboratory studies as well as in field observations on snow and ice composition. In light of the present results we pro-

ACPD
13, 30765–30839, 2013

vide an additional interpretation as follows: The higher $R_{ev}(H_2O)$ compared to $R_{ev}(HCl)$ leads to rapid evaporation of water from the forming ice sample that is two orders of magnitude larger than HCl, as shown in Fig. 6. This large difference between $R_{ev}(H_2O)$ and $R_{ev}(HCl)$ effectively explains the large enrichment of HCl in the condensed phase (ice) despite the large atmospheric abundance of H_2O vapour over HCl extending over several orders of magnitude.

In the present case we grew amHCl film by exposing a pure ice film of thickness in the range 1 to 2 µm (3 to 6×10^{18} molecules) to a total dose of approximately 3×10^{17} molecules of HCl at 175 K. Our samples are therefore a superposition of a bulk pure ice film with an amHCl film on top of it. As the abundance of H_2O decreases in the film, the spectroscopic characteristics of the film change as well, as presented in Fig. 15 where the temporal evolution of an amHCl film is shown under SFR conditions. A pure ice film (black spectrum) at 175 K is exposed to a flow of HCl of 1×10^{15} molec s^{-1} for roughly 10 min. Upon halting the HCl flow, the following spectral changes (purple spectrum) appear: a drastic decrease of the peak amplitude at 3233 cm^{-1} as well as an increasing shoulder at 3400 cm^{-1} and a broad band at 1700 cm^{-1} owing to the deposition of HCl. When deposition is stopped, the desired temperature for PV experiments is set. The spectrum continues to change even after halting the HCl flow, showing a further decrease of the peak at 3233 cm^{-1} (blue spectrum) in the aftermath of the first pulse of an HCl PV series at 175 K. As the temperature increases from 175 to 200 K more excess H_2O evaporates and the film loses the characteristic peak of pure ice at 3233 cm^{-1} and converts to a complete amorphous HCl/H_2O mixture film as shown by the red spectrum, albeit in lower intensity owing to evaporation of HCl and H_2O.

In Fig. 16 we have compared the complete amHCl films from Fig. 15 in the temperature range 187 to 200 K with the spectra recorded by Xueref and Dominé (2003). We only considered the spectra for the $HCl : H_2O$ gaseous mixtures of ratios 1 : 200 (black line) and 1 : 50 (grey line) as these are the spectra that come closest to the expected composition of the present samples. Indeed, this is the case since all spectra are fairly

ACPD
13, 30765–30839, 2013

similar. It therefore appears that all the present samples, once the excess H_2O has evaporated, are in the composition range 1 : 4 to 1 : 6 of $HCl : H_2O$.

5.6 Kinetic and thermodynamic aspects of HCl/H_2O phase diagram

The progress that the present work represents over a similar recent investigation into the $HCl \cdot 6H_2O$ vs. the amorphous HCl/H_2O phase lies in the thermochemical closure of the measured accommodation and evaporation kinetics of X in the presence of pure ice with the measured partial pressure of species X of the binary system X = HCl, H_2O. In other words, independent measurements of both $\alpha(X)$ and $R_{ev}(X)$ lead to the equilibrium vapor pressure $P_{eq}(X)$ given by the ratio $R_{ev}(X)/\alpha(X)$ which subsequently may be compared with independently measured values of $P_{eq}(X)$. This comparison in an overdetermined system is an excellent test of the self-consistency of the kinetic with the corresponding thermochemical parameters. At least for H_2O Figs. 6a and 8a provide good examples for the thermochemical consistency of the present data, both for pure ice (Marti and Mauersberger, 1993) as well as for $HCl \cdot 6H_2O$ and $amHCl/H_2O$ whose equilibrium vapor pressures are close to the ones for pure ice (Hanson and Mauersberger, 1990).

Figure 17a and b display both an Arrhenius plot of $J_{ev}(HCl)$ and van't Hoff plot of $P_{eq}(HCl)$ for the interaction of HCl with $amHCl/H_2O$ in comparison with results of an earlier Knudsen flow reactor study at steady-state addressing a slightly different region of the HCl/H_2O phase diagram, namely the HCl/H_2O liquid-ice coexistence region (Flückiger et al., 1998). The following equations define the corresponding straight lines based on the present (V/S = 1028.3 cm) as well as literature measurements (Flückiger et al., 1998; V/S = 122.0 cm) taking note of the conversion of evaporation rate and flux, namely, $R_{ev} \cdot V = J_{ev} \cdot A$ and $R = 8.314\,J\,K^{-1}\,mol^{-1}$. The best linear fit for the present measurements has been calculated using the iterative Levenberg–Marquardt least orthogonal distance method, that is minimizing the orthogonal distance of each point from the line of best fit. For the $amHCl/H_2O$ region (Eqs. 27 and 28) and ice/liquid

ACPD
13, 30765–30839, 2013

coexistence line (Eqs. 29 and 30) we find the following results:

$$\log J_{ev}(\mathrm{HCl})\ [\mathrm{cm^{-2}\,s^{-1}}] = (20.11 \pm 0.46) - (21.73 \pm 1.63) \times 10^3/(2.303 \cdot RT) \quad (27)$$

$$\log P_{eq}(\mathrm{HCl})\ [\mathrm{Torr}] = (4.55 \pm 0.39) - (35.76 \pm 1.38) \times 10^3/(2.303 \cdot RT) \quad (28)$$

$$\log J_{ev}(\mathrm{HCl})\ [\mathrm{cm^{-2}\,s^{-1}}] = (20.62 \pm 0.29) - (22.11 \pm 1.09) \times 10^3/(2.303 \cdot RT) \quad (29)$$

$$\log P_{eq}(\mathrm{HCl})\ [\mathrm{Torr}] = (1.92 \pm 0.29) - (27.05 \pm 1.11) \times 10^3/(2.303 \cdot RT) \quad (30)$$

J_{ev}(HCl) for amHCl/H_2O (red triangles) resulting from the present work is a factor of 2.6 smaller than for HCl adsorbed on ice either in the HCl/H_2O liquid phase or the H_2O-ice coexistence line as displayed by green squares in Fig. 17a. J_{ev}(HCl) for both of these slightly different areas of the phase diagram have been found to be identical (Flückiger et al., 1998). The kinetic results indicate that the slopes of both straight lines displayed in Fig. 17a corresponding to the activation energy for HCl evaporation are identical within the given uncertainties, namely 21.7 ± 1.6 (this work, Eq. 27) and $22.1 \pm 1.1\,\mathrm{kJ\,mol^{-1}}$ (Flückiger et al., 1998, Eq. 29). Although the evaporation process is identical in both cases it suggests that some structural or compositional parameters such as the abundance of H_2O on the surface must be different in both cases, thus accounting for the significant difference in the absolute values of J_{ev}(HCl), Eq. (27) vs. (29). The corresponding equilibrium vapor pressures $P_{eq}(\mathrm{HCl}) = R_{ev}(\mathrm{HCl})/\alpha(\mathrm{HCl})$, Eqs. (28) and (30) are in agreement with the published phase diagram (Molina, 1994) and point to a slightly higher value of the present data for amHCl/H_2O ($\Delta H^0_{ev}(\mathrm{HCl}) = 35.8 \pm 1.4\,\mathrm{kJ\,mol^{-1}}$) compared to the Flückiger data ($\Delta H^0_{ev}(\mathrm{HCl}) = 27.1 \pm 1.1\,\mathrm{kJ\,mol^{-1}}$) pertaining to the HCl/$H_2O$ liquid-ice coexistence line. Naively, one may think that the slightly higher value of ΔH_{ev}(HCl) of the present work suggests a slightly lower HCl concentration, i.e. slightly more diluted solution of the amHCl/H_2O of the present work compared to the Flückiger data on the basis of the data on HCl standard heats of solution (ΔH^0_{soln}(HCl)) given in Wagman et al. (1982).

However, one would expect a slightly larger absolute value for ΔH^0_{soln}(HCl) for the HCl/H_2O liquid-ice coexistence line compared to amHCl/H_2O. The caveat is that the

ACPD
13, 30765–30839, 2013

thermodynamic interpretation of the slopes in terms of ΔH^0_{ev} is not feasible because the coexistence line is the end point of a family of different HCl isoconcentration lines of the liquid domain at different temperatures. However, a thermodynamic value may be determined from the difference of activation energies for the evaporation (E_{ev}, Eq. 29) and accommodation (E_{acc}) rate of HCl on ice measured by Flückiger et al. (1998) and is calculated as $\Delta H^0_{ev} = \Delta H^0_{soln}(HCl) = 22.11 - (-7.53) = 29.64\,kJ\,mol^{-1}$ (Flückiger et al., 1998). This value is slightly larger than given in Eq. (30).

This value closely corresponds to ΔH^0_{ev} of a 1 : 1 $HCl : H_2O$ concentrated aqueous solution ending up on the ice-liquid coexistence line of the HCl/H_2O phase diagram (Wagman et al., 1982). When addressing the liquid domain of the phase diagram Flückiger obtained E_{ev} identical to the above value to E_{acc} measured as $-12.97\,kJ\,mol^{-1}$ such that $\Delta H^0_{ev}(HCl) = \Delta H^0_{soln}(HCl) = 22.11 - (-12.97) = 35.08\,kJ\,mol^{-1}$ was obtained which compares favorably with the exponential term of Eq. (28), namely $\Delta H^0_{ev}(HCl) = 35.76 \pm 1.38\,kJ\,mol^{-1}$.

Figure 18 presents an Arrhenius plot of $J_{ev}(HCl)$ of the crystalline phase over an extended temperature range that greatly exceeds the range covered by Chiesa and Rossi (2013) in their work on the decay of $HCl \cdot 6H_2O$ by following the IR absorption specific to the metastable hydrate at $3426\,cm^{-1}$. Equation (31) presents the two-parameter representation of the Arrhenius line ($J_{ev}(HCl)$) for crystalline $HCl \cdot 6H_2O$ and Eq. (32) recalls the Arrhenius line of Chiesa and Rossi (2013) using $V/A = 1506.4\,cm$:

$$\log J_{ev}(HCl)\,[cm^{-2}\,s^{-1}] = (38.02 \pm 4.82) - (87.03 \pm 16.96) \times 10^3/(2.303 \cdot RT) \quad (31)$$

$$\log J_{ev}(HCl)\,[cm^{-2}\,s^{-1}] = (36.31 \pm 1.65) - (80.83 \pm 6.01) \times 10^3/(2.303 \cdot RT) \quad (32)$$

A look at Fig. 18 reveals considerable scatter of the data of the Arrhenius plot which covers a fairly substantial temperature range compared to the Chiesa and Rossi (2013) data. The possible reasons for this scatter have been discussed above in the context of the kinetic parameters of $HCl \cdot 6H_2O$. This is reflected in the significant uncertainties of Eq. (31) compared to the work of Chiesa and Rossi (2013) despite the narrow tempera-

ACPD
13, 30765–30839, 2013

ture range covered in that work. Considering these differences the agreement between both data sets is seen to be very good so that we conclude that the rate-limiting step in the decay of $HCl \cdot 6H_2O$ is HCl evaporation, akin to the conclusions by Chiesa and Rossi (2013). This agreement between both methods is quite satisfying given the fact that Chiesa and Rossi followed the destruction of the condensed phase whereas the present work is conducted by observing the behavior of the gas phase in the presence of $HCl \cdot 6H_2O$.

A closer look at the data of Fig. 18 reveals that the observed positive T dependence of HCl evaporation may turn into a negative T dependence for $T < 172 \pm 2$ K which is the limit between the stable and metastable domain of $HCl \cdot 6H_2O$ (Chiesa and Rossi, 2013). It is possible that the limit of thermodynamic stability is in some way connected to the turn-over in the T dependence of the rate of HCl evaporation $R_{ev}(HCl)$ of $HCl \cdot 6H_2O$.

However, we are rapidly leaving the temperature range of atmospheric interest. The comparison between $E_{ev}(HCl)$ in $HCl \cdot 6H_2O$ of approximately $87.0 \pm 17.0\,kJ\,mol^{-1}$ following Eq. (31) has to be contrasted with the standard heat of sublimation of HCl calculated by Wooldridge et al. (1995) of $65.8\,kJ\,mol^{-1}$ at 200 K according to Reaction (R5), which however does NOT correspond to the usual definition of the standard heat of sublimation of a compound because H_2O stays in the condensed phase:

$$HCl \cdot 6H_2O \rightarrow HCl(g) + 6H_2O(s) \quad \text{(R5)}$$

This leads to an activation energy E_{ad} of HCl insertion or adsorption, the inverse process of Reaction (R5), of $E_{ad} = (87 \pm 17) - 65.8 = 21.2 \pm 17.0\,kJ\,mol^{-1}$, a decidedly positive activation energy in contrast to most other adsorption processes presented in this work. This peculiarity of an intrinsic positive activation energy for the inverse process has already been mentioned by Chiesa and Rossi (2013) and may have to do with the high value of activation energy $E_{ev}(HCl)$ out of the crystalline environment of $HCl \cdot 6H_2O$. In contrast, the corresponding activation energy E_{ad} for the case of the amorphous liquid is calculated as $E_{ad} = 21.7 - 35.8 = -14.1\,kJ\,mol^{-1}$ using Eqs. (27) and (28) which is expected behavior for this type of process.

ACPD
13, 30765–30839, 2013

Finally, a comparison between the absolute value of E_{ev} of the amHCl/H_2O (Eq. 27) and HCl·6H_2O (Eq. 31) may be considered. It is intuitively clear that HCl which is surrounded by H_2O molecules in a crystalline, albeit metastable hydrate shell may be more difficult to evaporate than HCl, either dissolved in a solution or adsorbed as a non-crystalline, that is amorphous phase. It is important to realize that the "border areas" of the "ice" solid phase containing HCl are in a disordered state (McNeill et al., 2006) and therefore cannot offer a crystalline environment to HCl. This means that the phase transition from the metastable crystalline (HCl·6H_2O) to a stable phase (am HCl/H_2O in both the "ice" and crystalline HCl·6H_2O phase domain) of constant composition will lead to an acceleration of J_{ev}(HCl) in contrast to the situation of the equilibrium vapor pressures displayed in Fig. 17a. It is satisfying that kinetic, thermodynamic and structural properties of the relevant portions of the HCl/H_2O phase diagram are conveying a unified physical picture based on as diverse experimental methods as used by McNeill et al. (2006) and the present kinetic/thermodynamic investigations.

5.7 Atmospheric implications

In this study we have confirmed the findings of Chiesa et al. (2013) that the structure of ice films (amorphous, polycrystalline, I_h) doped with HCl is irrelevant for the nucleation and growth of HCl·6H_2O. Furthermore, in agreement with previous studies (Ritzhaupt and Devlin, 1991; Koehler et al., 1993; Henson et al., 2004; Chiesa and Rossi, 2013), we have found that HCl·6H_2O requires a HCl supersaturation on the order of 10 or higher and temperatures $T \leq 173$ K to nucleate. Exposure of ice films to HCl at temperatures higher than 173 K, invariably led to the formation of an amorphous HCl/H_2O phase. The crystalline HCl·6H_2O has always been observed to convert to amorphous HCl/H_2O at temperatures $T > 193$ K under SFR conditions. On the other hand, the conversion of amorphous samples into crystalline HCl·6H_2O has never been observed under all explored experimental conditions.

On the basis of these observations we conclude that the nucleation of HCl·6H_2O is unlikely to occur under atmospheric conditions relevant for UT/LS, where the tempera-

ACPD
13, 30765–30839, 2013

tures are rarely less than 180 K. Furthermore, the high nucleation barrier for $HCl \cdot 6H_2O$ may be the reason for its kinetic instability leading to the inability of evaporating HCl to regenerate crystalline $HCl \cdot 6H_2O$ when it condenses back at atmospheric temperatures. The amorphous HCl/H_2O phase is likely to be the relevant phase in the processes involving HCl at UT/LS atmospherically relevant conditions.

6 Conclusions

In this work we have gone one step further compared to our recent work on the same subject using a stirred flow reactor (Chiesa and Rossi, 2013). The improvements may be summarized as follows: (1) combination of steady-state and transient supersaturation experiments in order to measure microscopic rates of evaporation R_{ev} and accommodation α, both for HCl and H_2O; (2) true multidiagnostic experiment, that is addressing gas- and condensed phase under identical reaction conditions, using FTIR absorption in transmission in order to label the kinetics of both HCl and H_2O with the corresponding FTIR absorption spectra; (3) spectral deconvolution of composite IR absorption spectra in terms of the concentration or mole fraction of HCl and H_2O such that each measured point in the HCl/H_2O phase diagram corresponded to a deconvoluted IR absorption spectrum.

The obtained kinetics of the forward (accommodation) and reverse (evaporation) experiments are consistent with the measured and/or previously known equilibrium vapour pressures. Among the most important experimental results that have been obtained under the constraint of thermochemical kinetics we cite (a) HCl accommodation and evaporation kinetics are significantly lower than for H_2O in the covered temperature range, both for $HCl \cdot 6H_2O$ and the amorphous mixture of HCl/H_2O. The phase transition from crystalline $HCl \cdot 6H_2O$ to the amorphous HCl/H_2O phase was controlled by the rate limiting step of HCl rather than H_2O evaporation. H_2O vapour seems to be a spectator that is adjusting easily owing to rapid kinetics; (b) the kinetics of HCl evaporation during the $HCl \cdot 6H_2O$ decay measured over an extended temperature range

ACPD
13, 30765–30839, 2013

closely corresponded to previous experiments in which the decay of the optical density of the crystalline $HCl \cdot 6H_2O$ was recorded, albeit over a restricted temperature range; (c) as a result of using the present multidiagnostic approach we have obtained an extension of the phase diagram in the existence area of crystalline $HCl \cdot 6H_2O$. However, this extension leaves the two known quadruple points from previous work unchanged, as expected.

Appendix A

According to the scheme presented in Eqs. (6)–(11), the following flow balance equation holds for a gas X (HCl, H_2O) in the stirred flow reactor (SFR):

$$F_{in}(X) + F_{des}(X) + F_{ev}(X) = F_{SS}(X) + F_{ads,w}(X) + F_{ads,ice}(X) \quad \text{(A1)}$$

where all terms are flow rates in molecs^{-1}. The interaction with the reactor walls is described by Langmuir type adsorption theory which assumes that a molecule can be adsorbed only on free specific surface sites.

The adsorption flux $J_{ads,w}$ in molecs^{-1}cm^{-2} is given by Eq. (A2) (Crowley et al., 2010):

$$J_{ads,w}(X) = \frac{\alpha_w(X) \cdot \bar{c}}{4}(1 - \theta) \cdot [X] \quad \text{(A2)}$$

where θ is the surface coverage, related to the surface concentration $[X]_S$ (in molecm^{-2}) as $[X]_S = \theta \cdot N_{MAX}$ with N_{MAX} representing the maximum number of molecules that can be adsorbed per cm^2.

The thermally activated desorption flux from the walls J_{des} may be expressed as follows if a first order rate law for desorption is assumed:

$$J_{des}(X) = k_{des} \cdot [X]_S = k_{des} \cdot \theta \cdot N_{MAX} \quad \text{(A3)}$$

ACPD
13, 30765–30839, 2013

Equilibrium is established when $J_{ads,w} = J_{des}$

$$\frac{\alpha_w(X)\cdot\bar{c}}{4}(1-\theta)\cdot[X] = k_{des}\cdot\theta\cdot N_{MAX} \quad (A4)$$

which may be expressed in the form of a Langmuir isotherm as

$$\theta = \frac{K_L[X]}{1+K_L[X]} \quad (A5)$$

with the Langmuir constant of partition coefficient K_L ($cm^3\,molec^{-1}$) given by:

$$K_L = \frac{\alpha_w(X)\cdot\bar{c}/4}{N_{MAX}\cdot k_{des,w}(X)} \quad (A6)$$

The desorption rate constant $k_{des,w}$ is calculated from Eq. (A6) as:

$$k_{des,w}(X) = \frac{\alpha_w(X)\cdot\bar{c}/4}{N_{MAX}\cdot K_L} \quad (A7)$$

with K_L, N_{MAX} and α_w measured for the SRF according to the methods described in Sects. 3.1 and 3.2. The flow balance Eq. (A1) may now be written as follow:

$$V\cdot R_{in}(X) + S_w\cdot N_{MAX}\cdot k_{des,w}(X)\cdot\theta + V\cdot R_{ev}(X) =$$
$$= V\cdot R_{SS}(X) + S_w\cdot\frac{\alpha_w(X)\cdot\bar{c}}{4}(1-\theta)\cdot[X] + S_{ice}\cdot\frac{\alpha_{ice}(X)\cdot\bar{c}}{4}\cdot[X] \quad (A8)$$

Substituting $S_w\cdot N_{MAX} = N_{TOT}$, the total number of molecules that can be adsorbed onto the total internal surface of the SFR, we may obtain Eq. (13).

ACPD
13, 30765–30839, 2013

Appendix B

In order to describe the temporal evolution of the total number of molecules N in the SFR reactor in the aftermath of a pulse experiment, we will first describe the simpler case with no ice and extend it afterwards to the case in the presence of ice. In the absence of an ice film, the scheme presented in Eqs. (6)–(11), can be simplified as follow for a gas X (X = HCl, H_2O):

$$\mathrm{X(g)} \rightarrow \text{escape} \qquad k_{\mathrm{esc}}(\mathrm{X})$$
(escape rate constant of X across reactor orifice) (B1)

$$\mathrm{X(ads)} \leftrightarrows \mathrm{X(g)} \qquad k_{\mathrm{w}}(\mathrm{X}), k_{\mathrm{des}}(\mathrm{X})$$
(rate constant of adsorption on and rate constant of desorption from reactor walls) (B2)

In the aftermath of a pulse the following rate equation holds:

$$\frac{\mathrm{d}N}{\mathrm{d}t} = F_{\mathrm{des}} - F_{\mathrm{esc}} - F_{\mathrm{ads}} \tag{B3}$$

where all terms are flow rates in molec s^{-1}. N is the total number of molecules inside the reactor, F_{des} the desorption flow rate from the reactor walls, F_{esc} the effusion rate across the orifice and F_{ads} the adsorption flow rate onto the reactor walls, respectively. The number of molecules N may be expressed as $N = [\mathrm{X}] \cdot V$, where V is the total volume of the SFR. The flow rates may be given in terms of fluxes as $F_y = J_y \cdot S$, where S is the internal surface of the reactor and J_y is the corresponding flux. According to Eqs. (A2) and (A3), Eq. (B3) may be expressed as:

$$\frac{\mathrm{d}N}{\mathrm{d}t} = S \cdot k_{\mathrm{des}} \cdot \theta \cdot N_{\mathrm{MAX}} - k_{\mathrm{esc}} \cdot N - S \cdot \frac{\alpha_{\mathrm{w}} \cdot \bar{c}}{4}(1-\theta) \cdot \frac{N}{V} \tag{B4}$$

ACPD
13, 30765–30839, 2013

In order to solve Eq. (B4) we assume that the desorption rate is low compared to adsorption processes so that at $t = 0$ there is no desorption from the walls. We may express the desorption term in Eq. (B4) as independent of N:

$$S \cdot k_{\mathrm{des}} \cdot \theta \cdot N_{\mathrm{MAX}} \cong k_{\mathrm{des}} \cdot N_{\mathrm{ADS}} \tag{B5}$$

Furthermore, we assume that the coverage is small ($\theta \ll 1$) and therefore the adsorption term in Eq. (B4) may be expressed as:

$$S \cdot \frac{\alpha_{\mathrm{w}} \cdot \bar{c}}{4}(1-\theta) \cdot \frac{N}{V} \cong S \cdot \frac{\alpha_{\mathrm{w}} \cdot \bar{c}}{4} \cdot \frac{N}{V} \tag{B6}$$

Equation (B4) may then be rewritten as:

$$\frac{\mathrm{d}N}{\mathrm{d}t} = k_{\mathrm{des}} \cdot N_{\mathrm{ADS}} - N \cdot b, \quad b = \left(k_{\mathrm{esc}} + \frac{S}{V} \cdot \frac{\alpha_{\mathrm{w}} \cdot \bar{c}}{4}\right) \tag{B7}$$

Equation (B7) is a differential equation that may be solved as sum of an homogeneous and inhomogeneous part.

The solution for the homogeneous part is as follows:

$$\frac{\mathrm{d}N}{\mathrm{d}t} = -N \cdot b$$

$$\int \frac{\mathrm{d}N}{N} = -\int b \cdot \mathrm{d}t$$

$$N(t) = C \cdot \mathrm{e}^{-bt} \tag{B8}$$

For the inhomogeneous part the solution may be found as follows:

$$N(t) = C(t) \cdot \mathrm{e}^{-bt} \tag{B9}$$

$$\frac{\mathrm{d}N}{\mathrm{d}t} = \frac{\mathrm{d}C}{\mathrm{d}t} \cdot \mathrm{e}^{-bt} - b \cdot C(t) \cdot \mathrm{e}^{-bt}$$

$$\frac{\mathrm{d}N}{\mathrm{d}t} = \frac{\mathrm{d}C}{\mathrm{d}t} \cdot \mathrm{e}^{-bt} - b \cdot N(t) \tag{B10}$$

ACPD
13, 30765–30839, 2013

From Eqs. (B7) and (B10) we may obtain:

$$k_{\mathrm{des}} \cdot N_{\mathrm{ADS}} - b \cdot N(t) = \frac{\mathrm{d}C}{\mathrm{d}t} \cdot \mathrm{e}^{-bt} - b \cdot N(t)$$

from which follows:

$$\frac{\mathrm{d}C}{\mathrm{d}t} = k_{\mathrm{des}} \cdot N_{\mathrm{ADS}} \cdot \mathrm{e}^{bt} \tag{B11}$$

We assume an exponential decay for N_{ADS}:

$$N_{\mathrm{ADS}} = N^0_{\mathrm{ADS}} \cdot \mathrm{e}^{-k_{\mathrm{des}}t} \tag{B12}$$

Equation (B11) may be integrated as follows:

$$\int \mathrm{d}C = k_{\mathrm{des}} \cdot \int N_{\mathrm{ADS}} \cdot \mathrm{e}^{bt} \cdot \mathrm{d}t \tag{B13}$$

which integrated by parts gives:

$$k_{\mathrm{des}} \cdot \int N_{\mathrm{ADS}} \cdot \mathrm{e}^{bt} \cdot \mathrm{d}t = k_{\mathrm{des}} \left(N_{\mathrm{ADS}} \cdot \frac{\mathrm{e}^{bt}}{b} - \int \frac{N_{\mathrm{ADS}}}{\mathrm{d}t} \cdot \frac{\mathrm{e}^{bt}}{b} \cdot \mathrm{d}t \right)$$

From Eq. (B12) we calculate the derivate of N_{ADS} and substitute, obtaining:

$$k_{\mathrm{des}} \cdot \int N_{\mathrm{ADS}} \cdot \mathrm{e}^{bt} \cdot \mathrm{d}t = k_{\mathrm{des}} \left(N_{\mathrm{ADS}} \cdot \frac{\mathrm{e}^{bt}}{b} + \frac{k_{\mathrm{des}}}{b} \cdot \int N_{\mathrm{ADS}} \cdot \mathrm{e}^{bt} \cdot \mathrm{d}t \right)$$

$$\left(1 - \frac{k_{\mathrm{des}}}{b}\right) \cdot k_{\mathrm{des}} \cdot \int N_{\mathrm{ADS}} \cdot \mathrm{e}^{bt} \cdot \mathrm{d}t = k_{\mathrm{des}} \cdot N_{\mathrm{ADS}} \cdot \frac{\mathrm{e}^{bt}}{b}$$

$$k_{\mathrm{des}} \cdot \int N_{\mathrm{ADS}} \cdot \mathrm{e}^{bt} \cdot \mathrm{d}t = \frac{k_{\mathrm{des}}/b \cdot N_{\mathrm{ADS}} \cdot \mathrm{e}^{bt}}{(1 - k_{\mathrm{des}}/b)} \tag{B14}$$

ACPD
13, 30765–30839, 2013

From Eqs. (B13) and (B14) we may obtain:

$$C(t) = \frac{k_{\mathrm{des}}/b \cdot N_{\mathrm{ADS}} \cdot \mathrm{e}^{bt}}{\left(1 - k_{\mathrm{des}}/b\right)} + C_0 \tag{B15}$$

And therefore obtain $N(t)$ in Eq. (B9):

$$N(t) = \frac{k_{\mathrm{des}}/b \cdot N_{\mathrm{ADS}}}{\left(1 - k_{\mathrm{des}}/b\right)} + C_0 \cdot \mathrm{e}^{-bt} \tag{B16}$$

At $t = 0$ we have $N(t) = N_0$, the number of molecules introduced with a pulse

$$C_0 = N_0 - \frac{k_{\mathrm{des}}/b \cdot N_{\mathrm{ADS}}}{\left(1 - k_{\mathrm{des}}/b\right)}$$

from which follows, together with Eq. (B12):

$$N(t) = N_0 \cdot \mathrm{e}^{-bt} + \frac{k_{\mathrm{des}}/b \cdot N^0_{\mathrm{ADS}} \cdot \mathrm{e}^{-k_{\mathrm{des}}t}}{\left(1 - k_{\mathrm{des}}/b\right)} \left(1 - \mathrm{e}^{-bt}\right) \tag{B17}$$

The solution presented in Eq. (B17) can be extended under the same assumptions to the case where ice is present by introducing a term similar to b that contains all loss processes:

$$d = \left(k_{\mathrm{esc}} + \frac{S}{V} \cdot \frac{\alpha_{\mathrm{w}} \cdot \bar{c}}{4} + \frac{S_{\mathrm{ice}}}{V} \cdot \frac{\alpha_{\mathrm{ice}} \cdot \bar{c}}{4}\right)$$

The governing equation in the presence of ice is:

$$\frac{\mathrm{d}N}{\mathrm{d}t} = k_{\mathrm{des}} \cdot N_{\mathrm{ADS}} + k_{\mathrm{ev}} \cdot N_{\mathrm{ev}} - N \cdot d \tag{B18}$$

ACPD
13, 30765–30839, 2013

where k_{ev} and N_{ev} are the rate constant of evaporation from the ice and the number of molecules adsorbed on the ice sample and evaporating from it, respectively.

With a mathematical derivation similar to the case in the absence of ice a solution for $N(t)$ can be derived as reported in Eq. (B19):

$$N(t) = N_0 \cdot e^{-dt} + \left(1 - e^{-dt}\right)\left(\frac{k_{des}/d \cdot N^0_{ADS} \cdot e^{-k_{des}t}}{\left(1 - k_{des}/d\right)} + \frac{k_{ev}/d \cdot N^0_{ev} \cdot e^{-k_{ev}t}}{\left(1 - k_{ev}/d\right)}\right) \quad \text{(B19)}$$

Equation (B19) represents the general solution for the fitting procedure of pulse experiments as a superposition of a fast decay given by the sum of all loss processes, $N_0 \cdot e^{dt}$, and a slower term which accounts for slower processes of evaporation from the ice and desorption from the walls.

Appendix C

Pulse fitting procedure

Figure C1 shows an example of the fitting procedure used to measure k_{ice} of HCl interacting with ice in the aftermath of a PV experiment. The grey line is the calibrated MS signal at m/z 36. Under the assumption that the desorption is slow compared to the fast adsorption processes it is possible to describe the decay of the signal as a sum of exponentials. A fast decay given by $k_d = k_{esc} + k_w + k_{ice}$ in the first 3 to 4 s after the pulse is superimposed on a slow desorption which becomes important once fast adsorption has subsided. The red curve shows a fit of a fast exponential decay associated to k_d. It is obvious that a simple adsorption process cannot accurately describe the behaviour of the measured signal, especially at longer decay times in the tail of the decay trace. The black curve shows a fit given by a superposition of a fast exponential decay k_d and a slower processes of evaporation from the ice and desorption from the walls. Good agreement is found with the measured calibrated signal of HCl.

ACPD
13, 30765–30839, 2013

All pulses measured during this work have been treated using the same assumptions and the best fit has been obtained for all decays in order to determine k_d and α_{ice} according to Eq. (21). Appendix B reports the mathematical derivation of the analytical form of the best fit of a pulse decay in the absence and in the presence of an ice sample.

Supplementary material related to this article is available online at http://www.atmos-chem-phys-discuss.net/13/30765/2013/acpd-13-30765-2013-supplement.zip.

Acknowledgement. The authors would like to acknowledge the unfailing and generous support of this work over the years by the Swiss National Science Foundation (SNSF) in the framework of projects 200020_125204 and 200020_144431/1. Moreover, we sincerely thank Alwin Frei for his support over the years the experiment was located in his laboratory.

References

Abbatt, J. P. D., Beyer, K. D., Fucaloro, A. F., McMahon, J. R., Wooldridge, P. J., Zhang, R., and Molina, M. J.: Interaction of HCl vapor with water-ice: implications for the stratosphere, J. Geophys. Res., 97, 15819–15826, 1992.

Banham, S. F., Sodeau, J. R., Horn, A. B., McCoustra, M. R. S., and Chesters, M. A.: Adsorption and ionization of HCl on an ice surface, J. Vac. Sci. Technol. A, 14, 1620–1626, 1996.

Broker, W. and Mossman, A. L.: Matheson Gas Data Book, 6th edn., Matheson Gas Products Inc., Lyndhurst, NJ, 1980.

Carslaw, K. S., Peter, T., and Clegg, S. L.: Modeling the composition of liquid stratospheric aerosols, Rev. Geophys., 35, 125–154, 1997.

Chiesa, S. and Rossi, M. J.: The metastable $HCl \cdot 6H_2O$ phase – IR spectroscopy, phase transitions and kinetic/thermodynamic properties in the range 170–205 K, Atmos. Chem. Phys. Discuss., 13, 17793–17848, doi:10.5194/acpd-13-17793-2013, 2013.

ACPD
13, 30765–30839, 2013

Chu, L. T., Leu, M.-T., and Keyser, L. F.: Uptake of HCl in water ice and nitric acid ice films, J. Phys. Chem., 97, 7779–7785, 1993.
Crowley, J. N., Ammann, M., Cox, R. A., Hynes, R. G., Jenkin, M. E., Mellouki, A., Rossi, M. J., Troe, J., and Wallington, T. J.: Evaluated kinetic and photochemical data for atmospheric chemistry: Volume V – heterogeneous reactions on solid substrates, Atmos. Chem. Phys., 10, 9059–9223, doi:10.5194/acp-10-9059-2010, 2010.
Deitz, V. R. and Turner, N. H.: Introduction of water vapor into vacuum systems and the adsorption by the walls, J. Vac. Sci. Technol., 7, 577–580, 1970.
Delval, C: Study of the kinetics of Condensation and Evaporation of Water Vapor over Atmospherically relevant Pure and Doped Ice Films: a Multidiagnostic Approach, Thèse EPFL no. 3159, 2005.
Delval, C., Fluckiger, B., and Rossi, M. J.: The rate of water vapor evaporation from ice substrates in the presence of HCl and HBr: implications for the lifetime of atmospheric ice particles, Atmos. Chem. Phys., 3, 1131–1145, doi:10.5194/acp-3-1131-2003, 2003.
Delzeit, L., Rowland, B., and Devln, J. P.: Infrared spectra of HCl complexed/ionized in amorphous hydrates and at ice surfaces in the 15–90 K range, J. Phys. Chem., 97, 10312–10318, 1993.
Dushman, S. and Lafferty, J. M.: Scientific Foundations of Vacuum Technique, 2nd Edn., ch. 1, John Wyley & Sons, 58 pp., New York, 1962.
Flückiger, B. and Rossi, M. J.: Common precursor mechanism for the heterogeneous reaction of D_2O, HCl, HBr and HOBr with Water Ice in the range 170–230 K: Mass accommodation coefficients on ice, J. Phys. Chem. A, 107, 4103–4115, 2003.
Flückiger, B., Thielmann, A., Gutzwiller, L., and Rossi, M. J.: Real time kinetics and thermochemistry of the uptake of HCl, HBr and HI on water ie in the temperature range 190 to 210 K, Ber. Bunsen. Phys. Chem., 102, 915–928, 1998.
Friedl, R. R., Goble, J. H., and Sander, S. P.: A kinetic study of the homogeneous and heterogeneous components of the $HCl + ClONO_2$ reaction, Geophys. Res. Lett., 13, 1351–1354, 1986.
Graham, J. D. and Roberts, J. T.: Formation of $HCl \cdot 6H_2O$ from ice and HCl under ultrahigh vacuum, Chemometr. Intell. Lab., 37, 139–148, 1997.
Hanson, D. R. and Mauersberger, K.: HCl/H_2O solid-phase vapor pressures and HCl solubility in ice, J. Phys. Chem., 94, 4700–4705, 1990.

ACPD
13, 30765–30839, 2013

Hanson, D. R. and Ravishankara, R.: Investigation of the reactive and nonreactive processes involving $ClONO_2$ and HCl on water and nitric acid doped ice, J. Phys. Chem., 96, 2682–2691, 1992.
Haynes, W. M., Bruno, T. J., and Lide, D. R. (Eds.): Handbook of Chemistry and Physics, 94th edn. (Internet Version 2014), CRC Press/Taylor and Francis, Boca Raton, FL, 2013.
Henson, B. F., Wilson, K. R., Robinson, J. M., Noble, C. A., Casson, J. L., and Worsnop, D. R.: Experimental isotherms of HCl on H2O ice under stratospheric conditions: connections between bulk and interfacial thermodynamics, J. Chem, Phys., 121, 8486–8499, 2004.
Huthwelker, T., Malmström, M. E., Helleis, F., Moortgat, G. K., and Peter, T.: Kinetics of HCl uptake on ice at 190 and 203 K: implications for the microphysics of the uptake process, J. Phys. Chem. A, 108, 6302–6318, 2004.
Hynes, R. G., Mössinger, J. C., and Cox, R. A.: The interaction of HCl with water-ice at tropospheric temperatures, Geophys. Res. Lett., 28, 2827–2830, 2001.
Koehler, B. G., McNeill, L., Middlebrook, A. M., and Tolbert, M. A.: Fourier transform infrared studies of the interaction of HCl with model polar stratospheric cloud films, J. Geophys. Res., 98, D6, 10563–10571, 1993.
Marti, J. and Mauersberger, K.: A survey and new measurements of ice vapor pressure at temperatures between 170 and 250 K, Geophys. Res. Lett., 20, 363–366, 1993.
McNeill, V. F., Loerting, T., Geiger, F. M., Trout, B. L., and Molina, M. J.: Hydrogen chloride-induced surface disordering on ice, P. Natl. Acad. Sci. USA, 103, 9422–9427, 2006.
McNeill, V. F., Geiger, F. M., Loerting, T., Trout, B. L., Molina, L. T., and Molina, M. J.: Interaction of hydrogen chloride with ice surfaces: the effects of grain size, surface roughness and surface disorder, J. Phys. Chem. A, 111, 6274–6284, 2007.
Molina, L. T., Molina, M. J., Stachnik, R. A., and Tom, R. D.: An upper limit to the rate of the $HCl + ClONO_2$ reaction, J. Phys. Chem., 89, 3779–3781, 1985.
Molina, M. J.: The probable role of stratospheric "ice" clouds: heterogeneous chemistry of the ozone hole, in: The Chemistry of the Atmosphere: Its Impact of Global Change, chapter 3, Blackwell Scientific Publications, London, 27–38, 1994.
Molina, M. J., Tso, T. L., Molina, L. T., and Wang, F. C. Y.: Antarctic stratospheric chemistry of chlorine nitrate, hydrogen chloride and ice: release of active chlorine, Science, 238, 1253–1257, 1987.
Peter, T.: Microphysics and heterogeneous chemistry of Polar Stratospheric Clouds, Annu. Rev. Phys. Chem., 48, 785–822, 1997.

ACPD
13, 30765–30839, 2013

Pouvesle, N., Kippenberger, M., Schuster, G., and Crowley, J. N.: The interaction of H_2O_2 with ice surfaces between 203 and 233 K, Phys. Chem. Chem. Phys., 12, 15544–15550, 2010.
Répánszki, R., Kerner, Z., and Nagy, G.: Adsorption of fission products on stainless steel and zirconium, Adsorption, 13, 201–207, 2007.
Ritzhaupt, G. and Devlin, J. P.: Infrared spectra of nitric and hydrochloric acid hydrate thin films, J. Phys. Chem., 95, 90–95, 1991.
Sadtchenko, V., Giese, C. F., and Gentry, W. R.: Interaction of hydrogen chloride with thin ice films: the effect of ice morphology and evidence for unique surface species on crystalline vapor-deposited ice, J. Phys. Chem. B, 104, 9421–9429, 2000.
Seinfeld, J. H. and Pandis, S. N.: Atmospheric Chemistry and Physics: From Air Pollution to Climate Change, ch. 5, 2nd edn., John Wiley & Sons, 2006.
Solomon, S., Garcia, R. R., Rowland, F. S., and Wuebbles, D. J.: On the depletion of Antarctic ozone, Nature, 321, 755–758, 1986.
Toon, O. B., Tolbert, M. A., Koehler, B. G., Middlebrook, A. M., and Jordan, J.: Infrared optical constants of H_2O ice, amorphous nitric acid solutions, and nitric acid hydrates, J. Geophys. Res., 99, 631–654, 1994.
von Hessberg, P., Pouvesle, N., Winkler, A. K., Schuster, G., and Crowley, J. N.: Interaction of formic and acetic acid with ice surfaces between 187 and 117 K. Investigation of single species- and competitive adsorption, Phys. Chem. Chem. Phys., 10, 2345–2355, 2008.
Wagman, D. D., Evans, W. H., Parker, V. B., Schumm, R. H., Halow, I., Bailey, S. M., Churney, K. L., and Nuttall, R. L.: NBS tables of chemical thermodynamic properties – selected values for inorganic and C_1 and C_2 organic substances in SI units, J. Phys. Chem. Ref. Data, 11, Suppl. 2, 1982.
Winkler, A. K., Holmes, N. S., and Crowley, J. N.: Interaction of methanol, acetone and formaldehyde with ice surfaces between 198 and 223 K, Phys. Chem. Chem. Phys., 4, 5270–5275, 2002.
Wooldridge, P. J., Zhang, R., and Molina, M. J.: Phase Equilibria of H_2SO_4, HNO_3 and HCl hydrates and the composition of polar stratospheric clouds, J. Geophys. Res., 100, 1389–1396, 1995.
Xueref, I. and Dominé, F.: FTIR spectroscopic studies of the simultaneous condensation of HCl and H2O at 190 K – Atmospheric applications, Atmos. Chem. Phys., 3, 1779–1789, doi:10.5194/acp-3-1779-2003, 2003.

ACPD
13, 30765–30839, 2013

Zondlo, M. A., Hudson, P. K., Prenni, A. J., and Tolbert, M. A.: Chemistry and microphysics of polar stratospheric clouds and cirrus clouds, Annu. Rev. Phys. Chem., 51, 473–499, 2000.

ACPD
13, 30765–30839, 2013

Table 1. Characteristic parameters of the used stirred flow reactor (SFR).

Reactor volume (upper chamber)	2036 cm^3
MS (lower) chamber	1750 cm^3
Reactor internal surface	1885 cm^2
HCl calibrated volume – inlet line	62 cm^3
H_2O calibrated volume – inlet line	44 cm^3
Si support area (one side)	$A_{Si} = 0.99\,cm^2$
Reactor wall temperature	$T_w = 315\,K$
Gas-surface collision frequency at 315 K, one side	7.39 s^{-1} (H_2O)
	5.22 s^{-1} (HCl)
$\omega = \frac{\bar{c}}{4V} \cdot A_{Si} = \sqrt{\frac{8RT}{\pi M}} \cdot \frac{A_{Si}}{4V}$ s^{-1} [a]	
Escape rate constant [b]	$C_S = 0.0408 \pm 0.0004$ (small orifice)
$k_{esc}^{SF} = C \cdot \sqrt{\frac{T}{M}}$ s^{-1}	$C_L = 0.161 \pm 0.002$ (large orifice)
	$C_{S+L} = 0.194 \pm 0.003$ (small + large orifice)

[a] M in kg; A_{Si} in m^2; V in m^3.
[b] M in g.

ACPD
13, 30765–30839, 2013

Table 2. Fit parameters for H_2O and HCl interaction with internal stainless steel surfaces (SS304) of the reactor.

	K_L^a [$cm^3\,molec^{-1}$]	N_{TOT} [molec]	N_{MAX} [$molec\,cm^{-2}$]
H_2O adsorption	$(3.18 \pm 0.38) \times 10^{-14}$	$(7.03 \pm 0.42) \times 10^{17}$	$(3.73 \pm 0.22) \times 10^{14}$
H_2O adsorption with HCl flow ($F_{in} = 8 \times 10^{14}$ molec s^{-1})	$(4.67 \pm 0.39) \times 10^{-14}$	$(8.38 \pm 0.29) \times 10^{17}$	$(4.45 \pm 0.15) \times 10^{14}$
HCl adsorption	$(4.37 \pm 0.21) \times 10^{-12}$	$(5.06 \pm 0.06) \times 10^{17}$	$(2.68 \pm 0.03) \times 10^{14}$
HCl adsorption with H_2O flow ($F_{in} = 6 \times 10^{15}$ molec s^{-1})	$(6.31 \pm 0.49) \times 10^{-13}$	$(4.85 \pm 0.07) \times 10^{17}$	$(2.57 \pm 0.04) \times 10^{14}$
HCl adsorption with H_2O flow ($F_{in} = 3 \times 10^{15}$ molec s^{-1})	$(6.46 \pm 0.63) \times 10^{-13}$	$(3.79 \pm 0.09) \times 10^{17}$	$(2.01 \pm 0.04) \times 10^{14}$

[a] K_L is the Langmuir adsorption equilibrium constant.

ACPD
13, 30765–30839, 2013

Table 3. Mass balance for selected experiments.

Exp	N^{FTIR} [molec] × 10^{17}	N_{in} [molec] × 10^{17}	N_{esc} [molec] × 10^{17}	N_{ads} [molec] × 10^{16}	Mass Balance Ratio[a]	Stoichiometry[b] (H_2O/HCl)
1	2.94 ± 0.86	5.19 ± 0.26	1.18 ± 0.06	6.73 ± 0.34	1.14	5.89
2	3.27 ± 0.96	6.00 ± 0.30	1.28 ± 0.06	9.99 ± 0.50	1.14	6.42
3	3.14 ± 0.92	6.09 ± 0.30	1.19 ± 0.06	7.78 ± 0.39	1.31	5.93
4	2.92 ± 0.85	5.48 ± 0.49	1.04 ± 0.05	6.31 ± 0.32	1.30	4.47
5	3.05 ± 0.89	4.79 ± 0.24	0.79 ± 0.04	8.95 ± 0.45	1.02	6.39

[a] Mass balance ratio is given by $(N^{in} - N^{esc} - N^{ads})/N^{FTIR}$.

[b] The average ratio of H_2O/HCl is 5.80 ± 0.70 taking into account all experiments. Excluding the outlier at 4.47 leads to an average ratio of 6.16 ± 0.29.

ACPD
13, 30765–30839, 2013

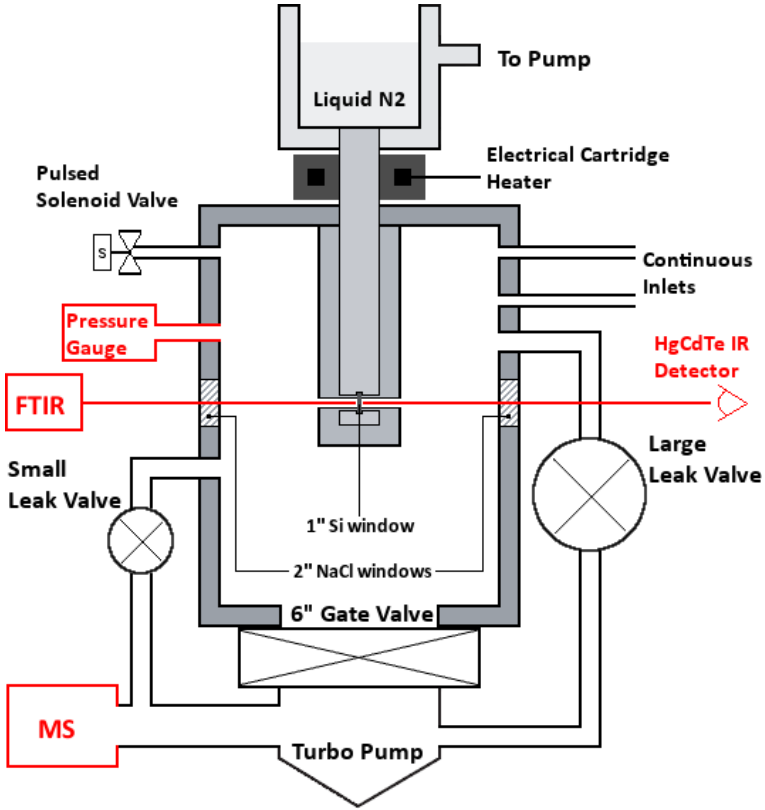

Fig. 1. Schematic drawing of the reactor used in this work. The diagnostic tools are highlighted in red and important parameters are listed in Table 1.

ACPD
13, 30765–30839, 2013

The HCl/H_2O phase diagram revisited

R. Iannarelli and
M. J. Rossi

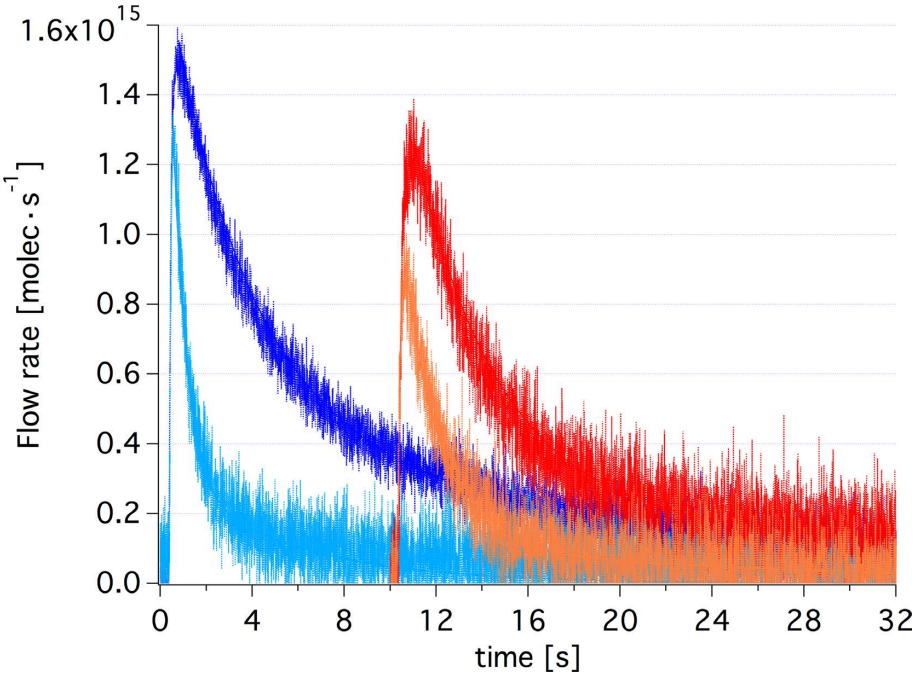

Fig. 2. Pulses of HCl and H_2O. The dark blue curve is a pulse of 1.5×10^{16} molecules of H_2O ($m/z = 18$) admitted into the reactor with the cryostat at $T_w = 315$ K for the measurement of uptake on the reactor walls. Likewise, the red curve is a pulse of 4.7×10^{16} molecules of HCl ($m/z = 36$) admitted into the reactor at $T_w = 315$ K. The light blue curve is a pulse of 2.7×10^{16} molecules of H_2O admitted in the presence of an HH film at 185 K, the orange curve is a pulse of 3.4×10^{16} molecules of HCl admitted in the presence of an HH film at 170 K. An offset of 10 s has been applied to the HCl curves for clarity.

ACPD
13, 30765–30839, 2013

The HCl/H_2O phase diagram revisited

R. Iannarelli and M. J. Rossi

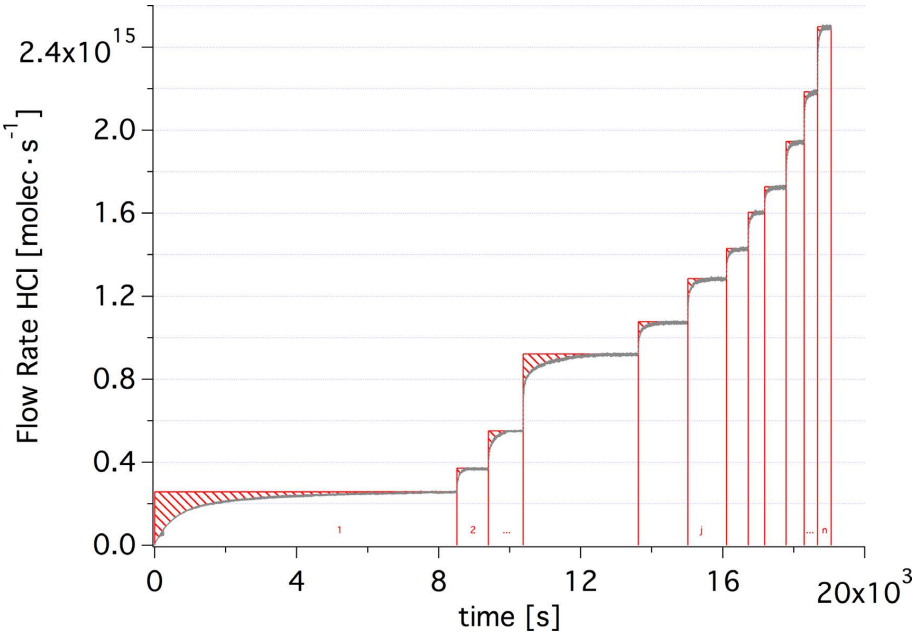

Fig. 3. Calibrated MS signal for the adsorption of HCl onto the stainless-steel reactor walls. The red shaded area represents the cumulative loss of molecules to the reactor walls at each j-th time interval as a function of the flow rate or partial HCl pressure.

ACPD
13, 30765–30839, 2013

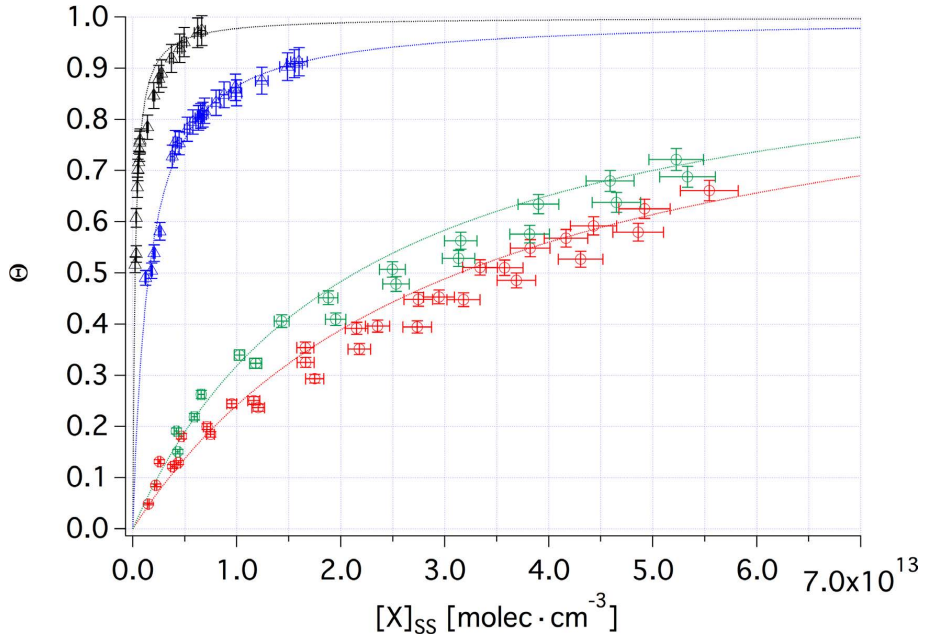

Fig. 4. Wall coverage as a function of HCl and H_2O concentration interacting with the reactor walls according to Langmuir using data of the type displayed in Fig. 3. The red symbols represent the interaction of pure H_2O and the green symbols the interaction of H_2O in the presence of an additional HCl flow $F_{in}(HCl) = 8 \times 10^{14}$ molecs^{-1} admitted into the reactor. Similarly, the black symbols represent the interaction of pure HCl, the blue symbols the interaction of HCl in the presence of an additional H_2O flow $F_{in}(H_2O) = (3 \div 6) \times 10^{15}$ molecs^{-1} admitted into the reactor. The parameters of the fitting curves may be found in Table 2.

ACPD
13, 30765–30839, 2013

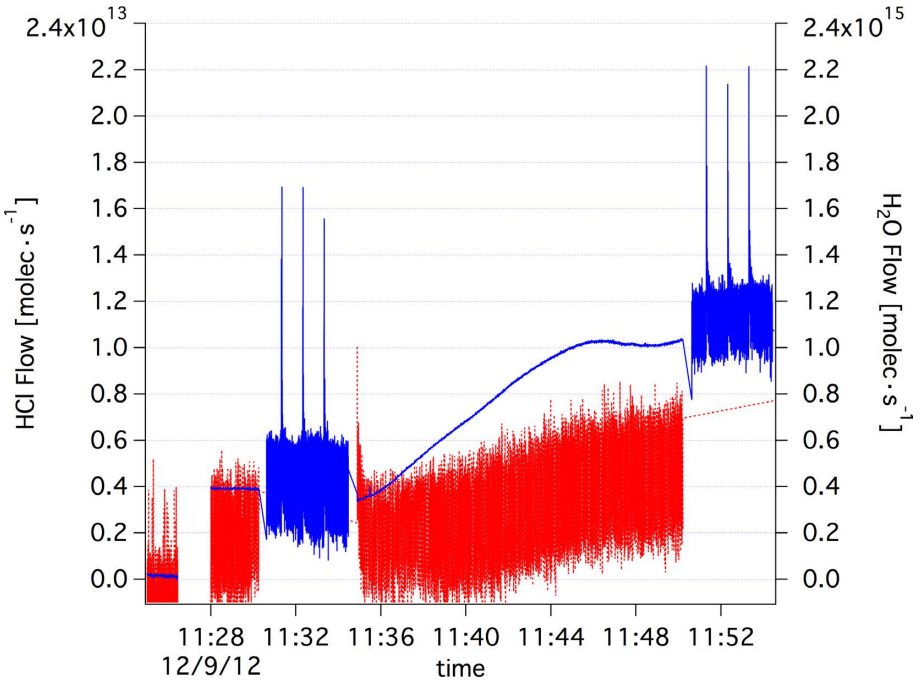

Fig. 5. PV and steady state experiment at low temperatures as a function of time on HH substrates. The blue curve (right axis) represents the H_2O flow rate with a series of pulses at 176 and 181.5 K. The red curve (left axis) represents the corresponding HCl flow rate at the same temperatures. The flows of HCl and H_2O at background are reported at the beginning of the time series for comparison. Similar results are obtained when pulses of HCl are admitted in the reactor. An example of HCl pulses in the presence of ice is displayed in orange in Fig. 2 compared to HCl pulses (red curve) in the absence of ice.

ACPD
13, 30765–30839, 2013

The HCl/H_2O phase diagram revisited

R. Iannarelli and M. J. Rossi

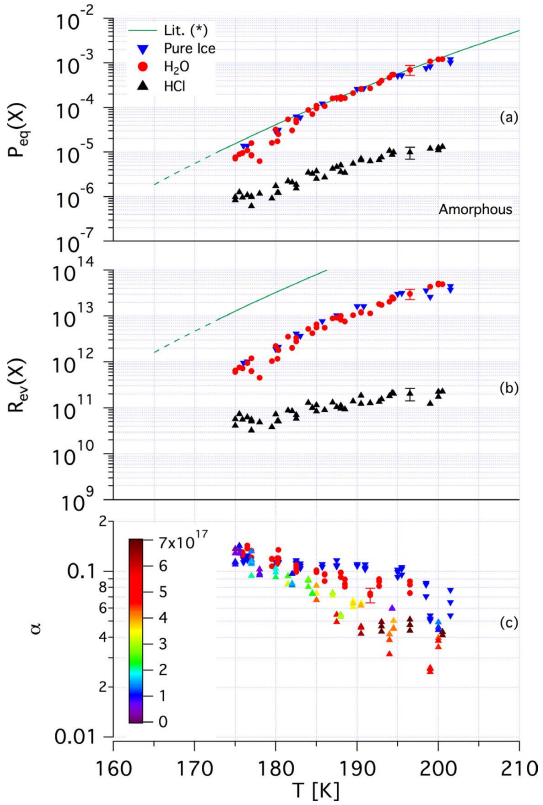

Fig. 6. Synopsis of kinetic results for amHCl using H_2O, HCl as a probe gas. The symbols used are explained in the text. The calculated relative error for α is 10 %. The relative errors calculated for R_{ev}(HCl) and P_{eq}(HCl) are 30 % whereas for $R_{ev}(H_2O)$ and $P_{eq}(H_2O)$ they are 25 %. Examples of the amplitude of the errors are reported for selected points. The green line shows results from Marti and Mauersberger (1993). The colour scale shows the cumulative adsorbed dose after HCl pulsed gas admission.

ACPD
13, 30765–30839, 2013

The HCl/H_2O phase diagram revisited

R. Iannarelli and M. J. Rossi

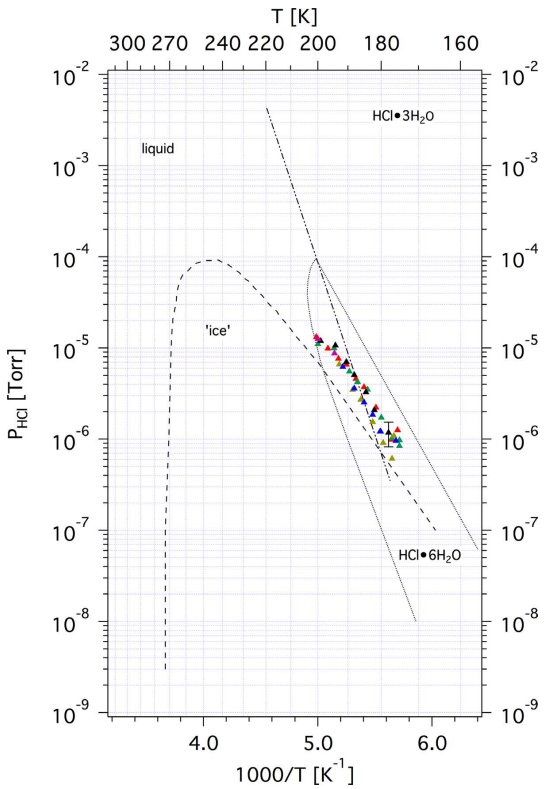

Fig. 7. Binary phase diagram of the HCl/H_2O system reconstructed from Molina and coworkers (Abbatt, 1992; Molina, 1994; Wooldridge, 1995). The full triangles represent calculated values of P_{eq}(HCl) for amHCl using the kinetic data of the present work. Different colours represent different experiment series.

ACPD
13, 30765–30839, 2013

The HCl/H_2O phase diagram revisited

R. Iannarelli and M. J. Rossi

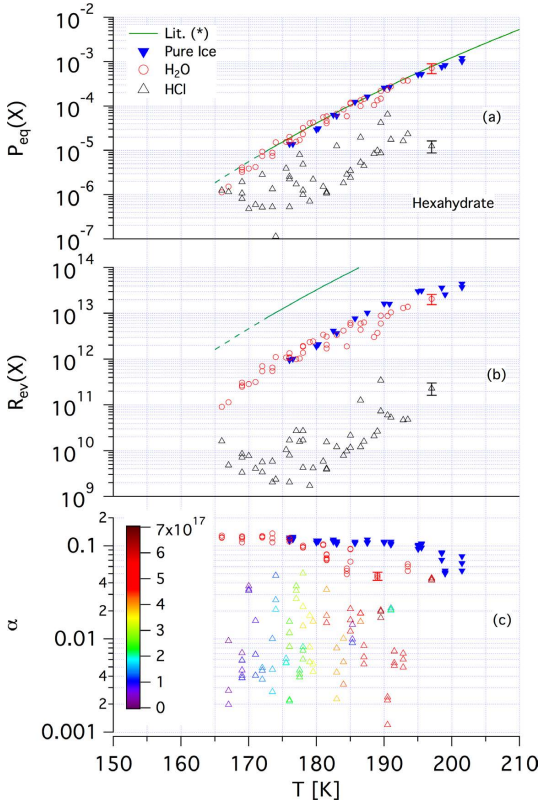

Fig. 8. Synopsis of kinetic results for HH using H_2O, HCl as a probe gas. The symbols used are explained in the text. The calculated relative error for α is 10 %. The relative errors calculated for R_{ev}(HCl) and P_{eq}(HCl) are 30 % whereas for R_{ev}(H_2O) and P_{eq}(H_2O) they are 25 %. Examples of the amplitude of the errors are reported for selected points. The green line shows results from Marti and Mauersberger (1993). The colour scale shows the cumulative adsorbed dose after HCl pulsed gas admission.

ACPD
13, 30765–30839, 2013

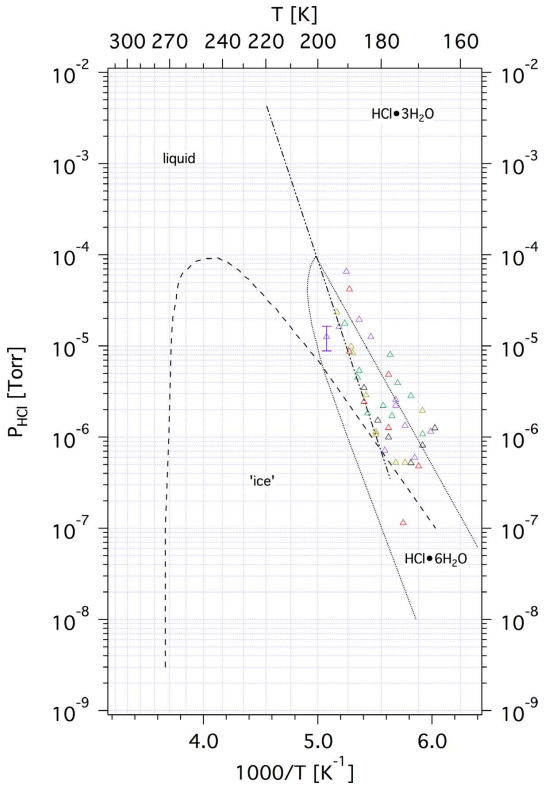

Fig. 9. Binary phase diagram of the HCl/H_2O system. The empty triangles represent calculated values of $P_{eq}(HCl)$ for HH using the kinetic data for adsorption and desorption of the present work. Different colours represent different experiment series.

ACPD
13, 30765–30839, 2013

The HCl/H_2O phase diagram revisited

R. Iannarelli and M. J. Rossi

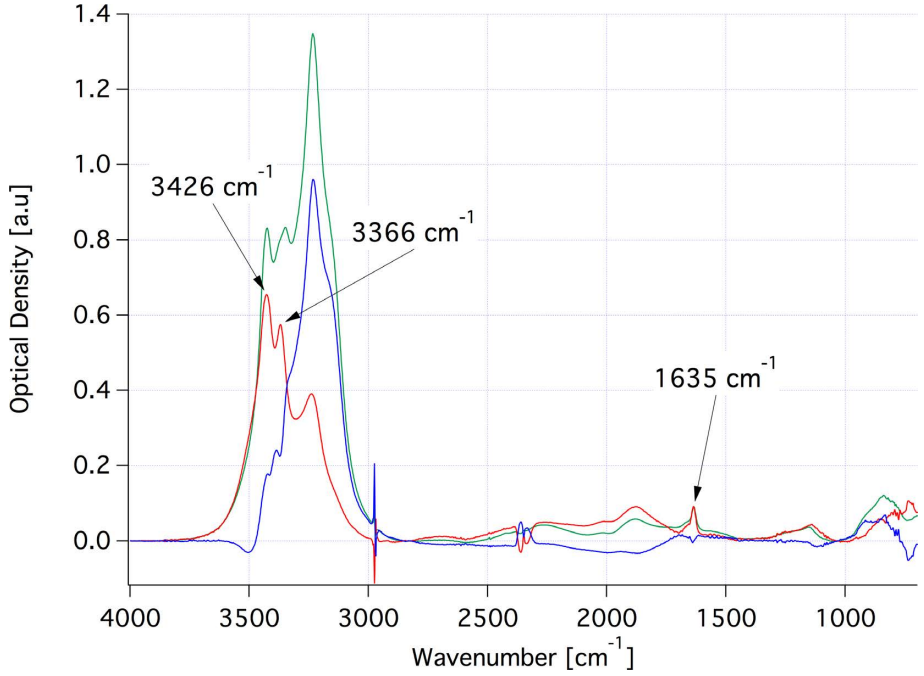

Fig. 10. Deconvolution of a measured FTIR absorption spectrum of a H_2O/HH mixture using its pure ice (blue) and pure HH (red) components. The measured composite FTIR absorption spectrum is shown in green.

ACPD
13, 30765–30839, 2013

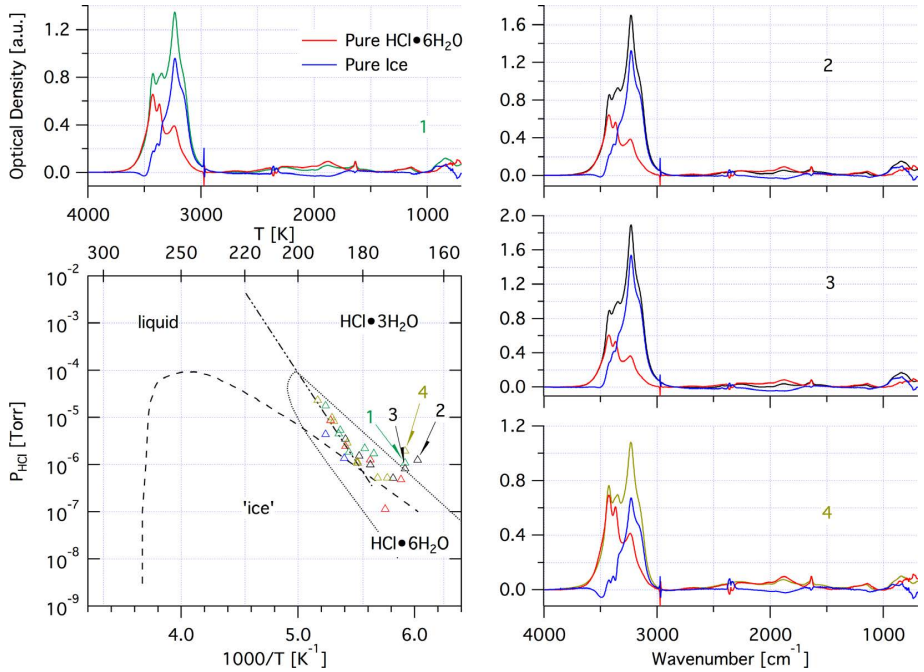

Fig. 11. Selected measured FTIR spectra with their deconvolution into pure ice (blue) and pure HH (red) component. The measured FTIR absorption spectra are coloured according to where they fit into the binary HCl/H_2O Phase Diagram.

ACPD
13, 30765–30839, 2013

The HCl/H_2O phase diagram revisited

R. Iannarelli and M. J. Rossi

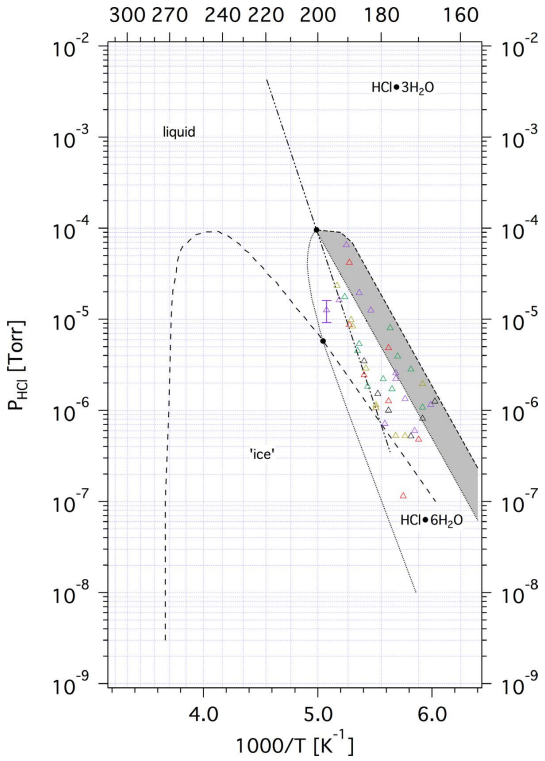

Fig. 12. Phase diagram of the HCl/H_2O system. The shaded area is the proposed extension of the HH existence area according to the results of the present work. The quadruple points (black dots) have been preserved.

ACPD
13, 30765–30839, 2013

The HCl/H_2O phase diagram revisited

R. Iannarelli and M. J. Rossi

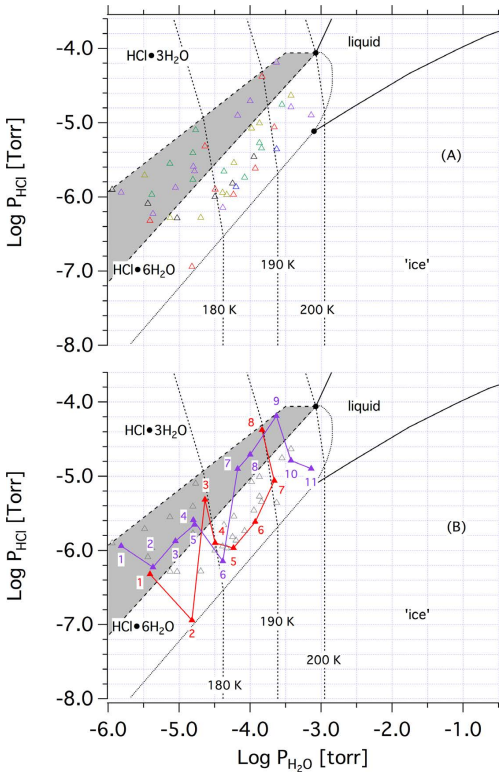

Fig. 13. Phase diagram of the HCl/H_2O system reconstructed from Hanson and Mauersberger, 1990. The empty coloured triangles represent calculated values of $P_{eq}(HCl)$ and $P_{eq}(H_2O)$ for HH using the kinetic results for adsorption and desorption of H_2O and HCl of the present work, according to Eq. (22). Different colours represent different experiment series. The shaded area is the proposed extension of the HH existence area according to the results of the present work with both quadruple points preserved. Panel **(B)** shows two different experiment series where the temporal evolution of the sample is discussed. Details may be found in the text.

ACPD
13, 30765–30839, 2013

The HCl/H_2O phase diagram revisited

R. Iannarelli and M. J. Rossi

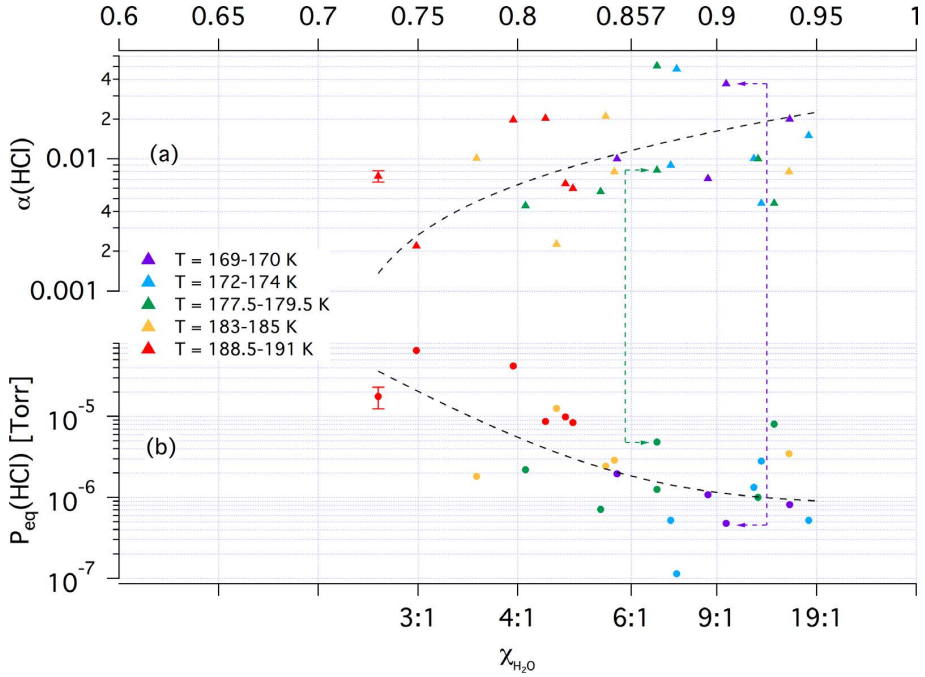

Fig. 14. P_{eq}(HCl) and α(HCl) as a function of mole fraction of H_2O in HH film. The bottom and top axes indicate the H_2O : HCl ratio and the H_2O weight percentage in the film, respectively. Colours identify different temperature ranges and the broken lines just serve to guide the eye. Coloured arrows indicate an example of pairs of data points.

ACPD
13, 30765–30839, 2013

The HCl/H_2O phase diagram revisited

R. Iannarelli and M. J. Rossi

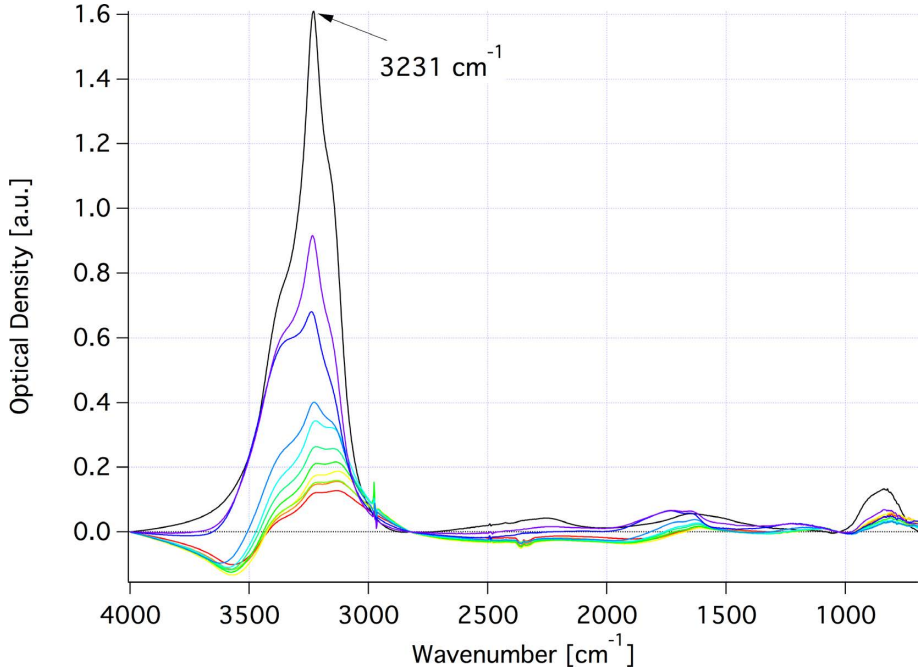

Fig. 15. Evolution of amHCl film. The spectrum of a pure ice film is represented in black and the conversion of an amHCl from a H_2O-rich film (purple spectrum) to an amorphous HCl/ice film (red spectrum) while pumping under SFR are displayed in colour. The spectra are colour-coded as a function of temperature in the range 175 to 200 K, with each spectrum corresponding to a temperature increase of roughly 3 K. All spectra from blue to red have been measured in the aftermath of the first pulse in a series of consecutive PV experiments.

ACPD
13, 30765–30839, 2013

The HCl/H_2O phase diagram revisited

R. Iannarelli and M. J. Rossi

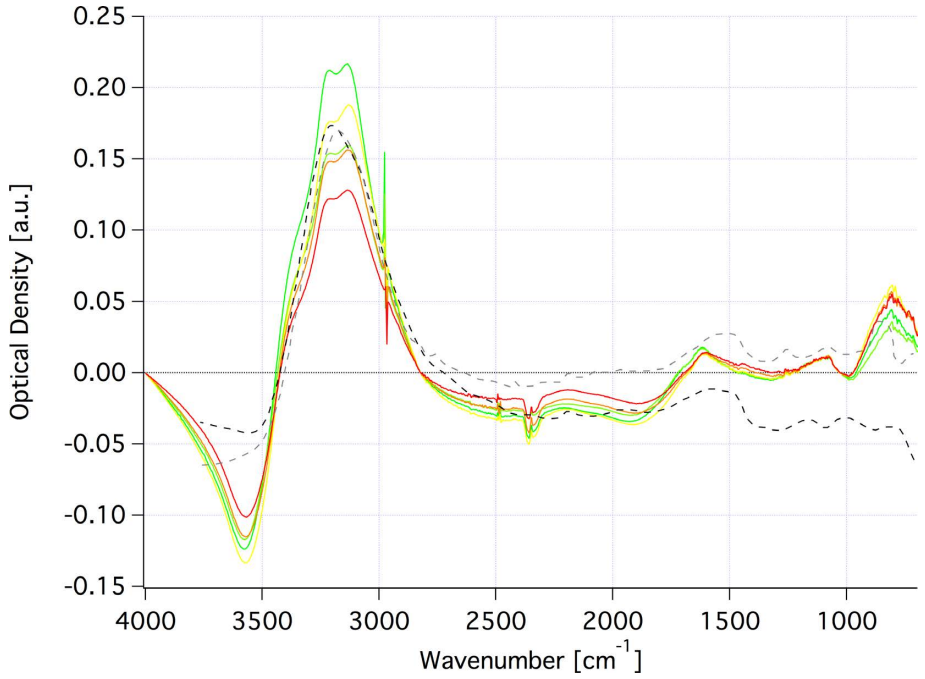

Fig. 16. Comparison of FTIR spectra of amHCl films. Our experimentally measured spectra are shown in colours according to temperature, whereas the dashed spectra correspond to samples made by condensing HCl : H_2O gaseous mixtures of ratios 1 : 200 (black line) and 1 : 50 (grey line) at 190 K of Xueref and Dominé (2003). The temperature of the ice sample ranges between 187 and 200 K with each spectrum measured in the aftermath of the first pulse in a series of PV experiments at temperature intervals of roughly 3 K.

ACPD
13, 30765–30839, 2013

The HCl/H_2O phase diagram revisited

R. Iannarelli and M. J. Rossi

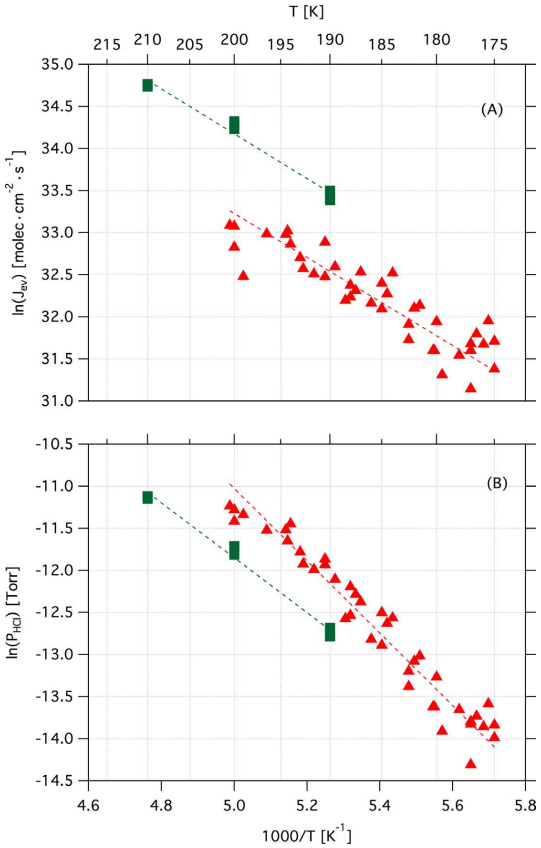

Fig. 17. Arrhenius plot of J_{ev}(HCl) **(A)** and van't Hoff plot of P_{eq}(HCl) **(B)**. Red triangles represent the results for the interaction of HCl with amHCl/H_2O down to T = 175 K (this study) and green squares the results from a Knudsen flow reactor study addressing the HCl/H_2O liquid-ice coexistence region (Flückiger et al., 1998). The equations for the fitting lines may be found in the text.

ACPD
13, 30765–30839, 2013

The HCl/H_2O phase diagram revisited

R. Iannarelli and
M. J. Rossi

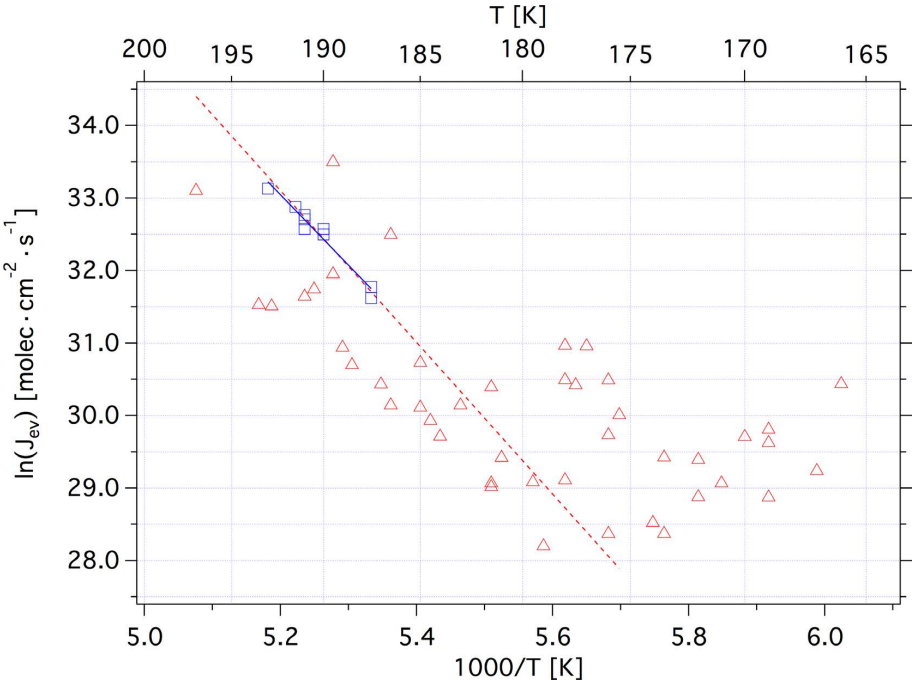

Fig. 18. Arrhenius plot of J_{ev}(HCl) for $HCl \cdot 6H_2O$. Red triangles represent the results of this study and blue squares the results of Chiesa and Rossi (2013) obtained from the decay of crystalline $HCl \cdot 6H_2O$. The equations for the linear fits may be found in the text.

ACPD
13, 30765–30839, 2013

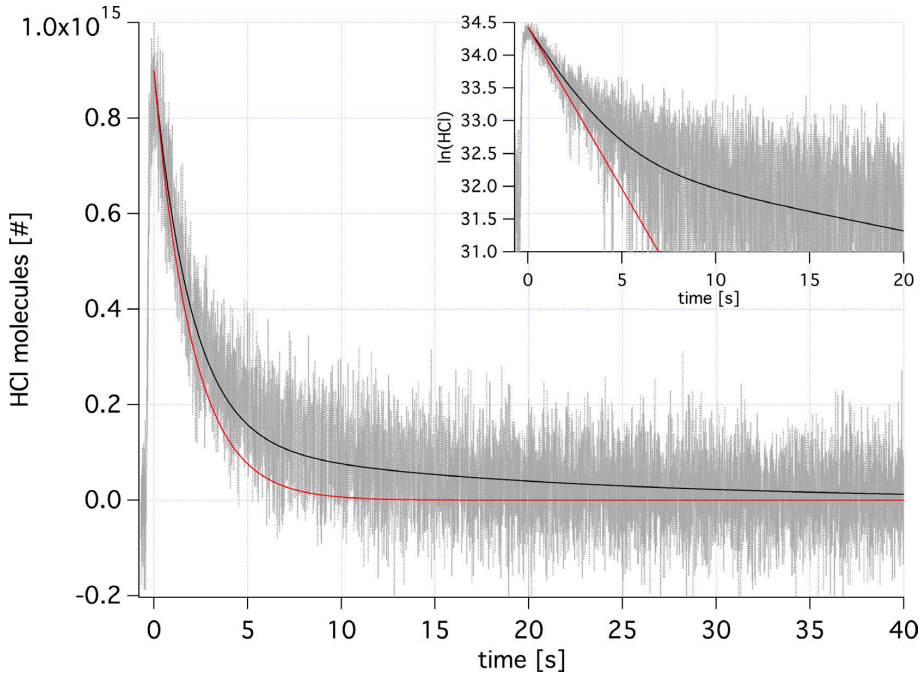

Fig. C1. Real time HCl PV experiment in the presence of ice at T = 189.5 K. The measured HCl calibrated signal is shown in grey as a function of time. In red and black fit curves of the signal. The red curve is calculated fitting the curve with an exponential decay whose constant is given by $k_d = k_{esc} + k_w + k_{ice}$. The black fit is calculated considering the signal decay as sum of a fast decay k_d and a slow desorption contribution from the walls and the ice. The insert shows the signal and the fits on a semi-logarithmic scale.

ACPD
13, 30765–30839, 2013